provides information about both the magnitude *and* the sign of an input parameter's sensitivity with respect to the output. An analysis of the strength and direction of each parameter's sensitivity can yield valuable guidance when making targeted model changes.

We note here that the analysis of high-sensitivity input parameters in this study does not solely rely on the output of the MOAT method. As applied in this study, the MOAT method serves as a tool to initially screen input parameters and identify those that produce relatively high sensitivity across a broad range of TC structural characteristics. To this end, a novel aspect of this study is the combination of sensitivity analysis, physical interpretation of input parameters, and practical considerations of modeling TCs in a global ESM. Importantly, we do not advocate for perturbing specific input parameters, which would require a more computationally expensive SA that is beyond the scope of this study.

Section 2 provides details about the idealized configuration of CAM6, including the CLUBB scheme, used in this study. This section also includes a description of the MOAT method, as well as the relevant inputs and outputs. Section 3 provides an analysis of the model sensitivities derived from the MOAT method, including an analysis of how this information can be applied to reduce biases in CAM6. Finally, conclusions are provided in section 4.

2. Data and methods

a. Model configuration

To isolate TCs from a more complex, fully coupled, climate, we apply an idealized model configuration. In particular, CAM6 is run in a configuration that closely mimics radiativeconvective equilibrium (RCE), a framework commonly used in modeling studies because it is a relatively simple, yet accurate, depiction of the tropical environment (Wing et al. 2018) and provides a controlled setup conducive to examining physical processes governing TC structure (Reed and Chavas 2015). We follow prior TC modeling studies (e.g., Held and Zhao 2008; Khairoutdinov and Emanuel 2013; Reed and Chavas 2015; Shi and Bretherton 2014; Wing et al. 2019; Zhou et al. 2014) in using a rotating RCE configuration in which we impart a constant Coriolis force (f plane) with an ambient rotation rate consistent with a latitude of 15°N. Our setup is similar to the rotating RCE framework in Reed and Chavas (2015), with a constant Coriolis force, spatially uniform, diurnally varying insolation, fixed SSTs set to approximately 302 K, no land or sea ice (i.e., an aquaplanet), uniform trace gas concentrations, and limited aerosol effects. Since we are interested in TC maintenance rather than genesis, we initialize CAM6 with a weak, symmetric vortex that is in hydrostatic and gradient wind balance, as described by Reed and Jablonowski (2012). An ensemble is created by randomly perturbing both the location (up to 0.1° in central latitude and longitude) and pressure deficit (up to 0.5 hPa) of the initial vortex k times.

Based on the advantages demonstrated in earlier studies (e.g., Zarzycki et al. 2014a,b; Zarzycki and Jablonowski 2014), we run CAM6 on a variable-resolution ne15×8 grid, which implies a spectral element (CAM-SE) grid with $n_e = 15$ (15 \times 15 elements per cubed sphere face) and a patch with a refinement factor of 8 (Zarzycki et al. 2014a). This refined resolution is comparable to the standard CAM-SE $n_e = 120$ grid, with an implied grid spacing of approximately 0.25°, or 25 km, which is consistent with other recent high-resolution ESM studies (e.g., Balaguru et al. 2020; Moon et al. 2020; Murakami et al. 2015; Reed and Chavas 2015; Roberts et al. 2020a,b; Wing et al. 2019). The refined domain is approximately $40^{\circ} \times 40^{\circ}$, which is sufficient for our analysis of a single TC per model run. We run CAM6 with 56 vertical levels in order to better resolve the TC PBL. We find that our results are also broadly applicable to a configuration with fewer vertical levels, such as the default 32-level configuration of CAM6 (see Fig. S1 in the online supplemental material). Within the sensitivity analysis, we run CAM6 with a physics time step $(dt_{\rm phys})$ of 450 s, 12 dynamics time steps per physics time step (se_nsplit = 12), and a vertical remap every tracer time step (se_rsplit = 1). These settings result in a dynamics time step (dt_{dyn}) of 37.5 s, which is intentionally set to a low value to ensure numerical stability for the variety of previously untested parameter combinations explored in the MOAT analysis. However, we note that a handful of configurations require a smaller dt_{dyn} , depending on the exact settings of tunable parameters. In these cases, stability is achieved by halving the $dt_{\rm dyn}$ to 18.75 s. We find that halving the $dt_{\rm dyn}$ does not appreciably alter results for otherwise stable configurations (Fig. S2). Outside of the MOAT analysis, we run the CAM6 simulations with a dt_{dyn} of 112.5 s (se_nsplit = 4). All CAM6 simulations are integrated for 16 days.

We also introduce a modification to the formulation of the surface drag coefficient C_D , which in CESM2 is based on the formula from Large and Pond (1981). However, at high 10-m wind speeds this formulation produces a value of C_D that monotonically increases as wind speed increases. Despite quantitative uncertainties in observations (Richter et al. 2021), numerous studies have demonstrated that C_D likely levels off (saturates) or decreases at high 10-m wind speeds, such as those typical of mature TCs (e.g., Bye and Jenkins 2006; Donelan et al. 2004; Makin 2005; Moon et al. 2008; Powell et al. 2003). To better simulate the observed saturation of C_D at high wind speeds in TCs, we retain the default formulation of C_D but enforce it to be constant at 10-m wind speeds in excess of a chosen wind speed threshold (Donelan et al. 2004). Large and Yeager (2009) applied a smoothed cutoff at 33 m s⁻¹ by adding an additional high-order exponential decay term to the Large and Pond (1981) formulation. Since this term is tailored to the specific threshold of 33 m s⁻¹, we apply a discrete cutoff instead to allow for easier perturbation of the threshold.

b. PBL scheme

In CAM6, the CLUBB scheme serves as a unified parameterization for stratiform macrophysics, shallow convection,

and PBL turbulence. This scheme selects a joint probability density function (PDF) of vertical velocity, temperature, and moisture from a family of PDFs and achieves closure of higher-order turbulent moments and buoyancy terms by integrating over the chosen PDF, which takes the form of a double Gaussian (Golaz et al. 2002). Zarzycki and Jablonowski (2015) demonstrated the potential utility of CLUBB in ESM TC hindcasts, as they showed that including CLUBB in CAM5 reduced track errors compared to a configuration without CLUBB. Meanwhile, CAM5 with CLUBB was more skillful in predicting 10-m wind speed beyond 72 h compared to CAM5 without CLUBB, with CAM5-CLUBB providing a 40% increase in relative wind speed skill at 120 h. Nonetheless, CAM5-CLUBB still had notable biases in both track and intensity hindcasts. Since Zarzycki and Jablonowski (2015) only implemented an older version of CLUBB in a previous version of CAM, this study will provide novel insights into the performance of CAM6 and CLUBB with respect to TCs.

One noted drawback of CLUBB is that the vertical momentum fluxes $\overline{u'w'}$ and $\overline{v'w'}$ have not traditionally been prognosed, but instead have been diagnosed by assuming simple downgradient fluxes:

$$\overline{u'w'} = -K_m \frac{\partial \overline{u}}{\partial z},\tag{1}$$

$$\overline{v'w'} = -K_m \frac{\partial \overline{v}}{\partial z}.$$
 (2)

Here and elsewhere in the text, bars represent the gridbox mean, while prime superscripts represent the perturbation from the gridbox mean. The term K_m is a varying eddy diffusivity coefficient defined as follows:

$$K_m = c_k L \overline{e}^{1/2}, \tag{3}$$

where L is the vertical turbulent length scale, \bar{e} is the turbulent kinetic energy, and c_k is a constant set to 0.5.

However, recent studies have suggested that the downgradient approach is inadequate because it neglects observed countergradient fluxes, such as those demonstrated by Larson et al. (2019) in tropical shallow cumulus cases from the Barbados Oceanographic and Meteorological Experiment (BOMEX) campaign. They noted that the upgradient fluxes are likely due to buoyancy production or turbulence advection terms that are not included in the downgradient formulation. Although turbulence in the TC PBL is expected to be mostly shear-generated (e.g., Kepert 2001), there is evidence that upgradient fluxes exist in the TC PBL. For example, Kepert (2012) demonstrated that PBL schemes parameterizing momentum flux using the downgradient assumption did not accurately predict vertical wind profiles in the TC PBL, while Persing et al. (2013) found that upgradient fluxes occur in the TC PBL in high-resolution 3D simulations. Therefore, we apply an experimental version of CLUBB (hereafter referred to as CLUBBX) that employs a more realistic prognostic equation for momentum flux. Specifically, CLUBBX solves the following budget equation for the local time variation of momentum flux (Larson et al. 2019):

$$\frac{\partial \overline{u'w'}}{\partial t} = \underbrace{-\overline{w}}_{1} \underbrace{\frac{\partial \overline{u'w'}}{\partial z}}_{1} - \underbrace{\frac{1}{\rho}}_{2} \underbrace{\frac{\partial \rho \overline{w'^{2}u'}}{\partial z}}_{2} - \underbrace{(1 - C_{7upwp})\overline{w'^{2}}}_{3} \frac{\partial \overline{u}}{\partial z} \\
- \underbrace{(1 - C_{7})\overline{u'w'}}_{4} \underbrace{\frac{\partial \overline{w}}{\partial z}}_{2} + \underbrace{(1 - C_{7})\frac{g}{\theta_{us}} \overline{u'\theta'_{v}}}_{5} \\
- \underbrace{\frac{C_{6}}{\tau} \overline{u'w'}}_{7} - \underbrace{\epsilon_{uw}}_{7}.$$
(4)

Here, g represents gravitational acceleration, τ represents the eddy turnover time scale (Larson 2020), θ_v represents the virtual potential temperature, θ_{us} represents the basic-state virtual potential temperature, $\rho(z)$ represents average air density, and C_6 and C_7 are tunable constants between 0 and 1. Per Larson et al. (2019), the terms on the rhs of the budget in Eq. (4) represent: 1) advection of momentum flux $\overline{u'w'}$ by the mean vertical wind \overline{w} , 2) turbulent advection of momentum flux by the vertical perturbation velocity w', 3) turbulent production of momentum flux by updrafts and downdrafts, 4) turbulent production of momentum flux due to existing momentum flux in the presence of a vertical gradient in mean vertical wind \overline{w} , 5) buoyant production of momentum flux, 6) a return-to-isotropy adjustment that reduces the magnitude of momentum flux, and 7) additional dissipating processes. The momentum flux budget in Eq. (4) is based on CLUBBX's formulation of the scalar flux budgets $\overline{w'\theta'}$ and $\overline{w'q'}$ [Eqs. (16) and (17) in Golaz et al. (2002)]. However, our Eq. (4) has an additional pressure term $[C_{7upwp} \overline{w'^2} (\partial \overline{u}/\partial z)]$ that offsets the turbulent production of momentum flux from updrafts and downdrafts. Like C_6 and C_7 , C_{7upwp} is a tunable constant between

With prognostic momentum flux turned on, the eddy diffusivity coefficient K_m in Eq. (3) is no longer used in the calculation of momentum flux. However, to quantify the degree of vertical mixing in the subsequent analysis, we follow Bryan et al. (2017) and recast K_m as an effective eddy diffusivity:

$$K_{m} = \frac{\sqrt{(\overline{v'w'})^{2} + (\overline{v'w'})^{2}}}{\sqrt{\left(\frac{\partial \overline{u}}{\partial z}\right)^{2} + \left(\frac{\partial \overline{v}}{\partial z}\right)^{2}}}.$$
 (5)

This formulation is also consistent with estimates of K_m used in observational studies (e.g., French et al. 2007; Ueda et al. 2012; Zhang and Drennan 2012).

An additional modification to how CLUBBX calculates the turbulent length scale L (Guo et al. 2021) is also used here (all references in this paper are to the *vertical* turbulent length scale). CLUBB typically estimates L by calculating how far upward and downward a parcel can travel due to buoyancy effects (Golaz et al. 2002; Larson 2020). Here, we diagnose the turbulent length scale using τ , the eddy turnover time scale, and the turbulent kinetic energy (TKE): $L = \tau \bar{e}^{1/2}$ (Larson 2020). We derive τ from the inverse eddy turnover time scale $1/\tau$ (Guo et al. 2021):

$$\frac{1}{\tau} = \underbrace{C_{\text{bkgnd}}}_{1} \frac{1}{\alpha} + \underbrace{\frac{C_{\text{sfc}} u^{*}}{\kappa} \frac{1}{(z - z_{\text{sfc}} + d)}}_{2} + \underbrace{C_{\text{shear}} \sqrt{\left(\frac{\partial \overline{u}}{\partial z}\right)^{2} + \left(\frac{\partial \overline{v}}{\partial z}\right)^{2}}}_{3} + \underbrace{C_{N2} \sqrt{N^{2}}}_{4}, \tag{6}$$

where $\alpha = 1000 \text{ s}^{-1}$ is a constant, u^* is the friction velocity (m s⁻¹), $\kappa = 0.4$ is Von Kármán's constant, z is the model height (m), $z_{\rm sfc}$ is the surface elevation (m), d is the displacement depth (m), N is the Brunt Väisälä frequency (s^{-1}), and the C_x coefficients on the rhs are tunable constants, which are referenced in the text as C_invrs_tau_bkgnd, C_invrs_tau_sfc, C_invrs_tau_shear, and C_invrs_tau_N2, respectively. Since τ is directly proportional to L, $1/\tau$ is formulated as the sum of various dissipating processes in the TC PBL where increasing $1/\tau$ decreases L, which physically represents the breakup of larger turbulent eddies (greater L) into smaller turbulent eddies (lower L). The terms on the rhs of Eq. (6) represent: 1) a generic background dissipation of turbulent eddies applied at all levels, 2) dissipation near the surface due to frictional effects, 3) dissipation due to vertical wind shear, and 4) dissipation in a stable atmosphere. The benefit of this modified formulation for $1/\tau$ and L is that it can be adjusted at the regime level via the tuning of the four coefficients on the rhs of Eq. (6). This study presents the first analysis of how these dissipation coefficients influence PBL turbulence in TCs.

c. Sensitivity analysis

To test the relative influence of PBL parameters on TC structure, we apply the MOAT method, which was first introduced by Morris (1991) and later refined by Campolongo et al. (2007). Recently, the MOAT method has gained wider use in the field of atmospheric science. For instance, Covey et al. (2013) applied the MOAT method to analyze the influence of 27 input parameters on radiative fluxes in CAM3 and CAM4. Morales et al. (2019) later used the MOAT method to evaluate the influence of 19 microphysical and thermodynamic parameters on orographic precipitation characteristics in a high-resolution, cloud-resolving model. Zarzycki and Ullrich (2017) also applied the MOAT method to the objective detection of extreme weather, as they evaluated the effect of perturbing 12 input parameters on the number and intensity of TCs detected by the TempestExtremes tracking algorithm.

Aside from being well-vetted, the MOAT method effectively analyzes sensitivity in a computationally efficient manner. In fact, Herman et al. (2013) compared the performance of the MOAT method with the commonly used Sobol method in screening parameters in a watershed model and found that MOAT produced similar results with approximately 300 times fewer computing hours and 180 times less required storage. Also, unlike other computationally efficient one-at-a-time (OAT) methods that compare sensitivities to the same baseline configuration, the MOAT method varies the baseline configuration, which is appropriate for nonlinear climate systems where parameter sensitivities may vary between baseline

climate states (Covey et al. 2013). However, we also note some drawbacks of the MOAT method. For example, the MOAT method alone cannot quantify the fraction of the output variance explained by each parameter, which would require a more computationally expensive procedure (Morales et al. 2019). In addition, the MOAT method does not cover the entire set of possible combinations of input values. However, we feel that the benefits of the MOAT method outweigh the drawbacks given the goal of our study, to provide an initial identification of high-sensitivity input parameters in modeling the structure of the TC PBL.

The MOAT method, which has recently been described in detail by Covey et al. (2013) and Morales et al. (2019), is briefly summarized here. Like other SAs, the MOAT method works by quantifying changes in an output metric y given a change in an input parameter x_i . The process begins with an initial model configuration that has a set of input parameters $X = \{x_1, x_2, \dots, x_i, \dots, x_N\}$. Each input x_i is randomly assigned a value from a discrete range of plausible values. CAM6 (hereafter referred to as CAM6-CLUBBX) is then run with this particular combination of input parameter values. CAM6-CLUBBX is subsequently run with a second combination of N input parameter values, generated by taking the first combination and changing the value of only one input parameter. The procedure continues until all N input parameter values have been changed once, one-at-a-time. This process, called a MOAT "path," is repeated M times with a new initial combination of input parameter values each time. In this way, each path starts with a unique baseline state, thus allowing the analysis to account for the dependence of the sensitivities on baseline state (Covey et al. 2013). The MOAT method requires M(N + 1) total model runs, which is significantly smaller than the M^N model runs required for a standard multiparameter SA (Morales et al. 2019).

The output from the M(N + 1) model runs is used to calculate "elementary effects," which quantify the change in y due to a positive change in x_j , within a given path i:

$$d_{ij} = \frac{y(x_1, x_2, ..., x_j + \Delta, ..., x_N) - y(x_1, x_2, ..., x_j, ..., x_N)}{\Delta}.$$
 (7)

Here, Δ represents the magnitude of the change in the input parameter. Δ is standardized to allow for an easier comparison between input parameters with different units. For each input-output pair, sensitivity metrics can be derived by calculating the mean and standard deviation of the elementary effects over all M paths (Covey et al. 2013). The term μ_i^* is a measure of the average change in output metric y when perturbing the *j*th input parameter. Meanwhile, σ_i is a measure of the variability of the change over the sampled baseline states, either due to the input parameter's own nonlinear effects or the input parameter's nonlinear interactions with other input parameters (Covey et al. 2013; Morales et al. 2019). We also introduce a new quantity, the "monotonicity" of the response of output y to input x_i (denoted by f_{i+}). Since the Δ term in (7) is always positive, f_{i+} is the probability, over the M paths, that increasing the input parameter increases the output:

	Input ID	Description	Default	Range
C14	Α	Coefficient for u and v variance terms	2.2	1 - 4
C7	В	Coefficient for production and buoyancy terms in turbulent scalar flux budget	0.5	0.35 - 0.80
C7upwp	С	Additional coefficient for turbulent production in momentum flux budget	0.5	0.35 - 0.80
C6rt Lscale0	D	Damping term used to derive return-to-isotropy term in turbulent scalar flux budget	14	10 - 15
	E	Coefficient for return-to-isotropy term in w variance budget	5.2	3 - 7
C_invrs_tau_bkgnd	F	Coefficient tied to background eddy dissipation in formulation of turbulent length scale	1.0	0.5 - 4.0
C_invrs_tau_sfc	G	Coefficient tied to eddy dissipation near the surface in formulation of turbulent length scale	0.1	0.05 - 0.40
C_invrs_tau_shear	Н	Coefficient tied to eddy dissipation from wind shear in formulation of turbulent length scale	0.02	0.01 - 0.06
C_invrs_tau_N2	1	Coefficient tied to eddy dissipation from buoyancy in formulation of turbulent length scale	0.1	0.05 - 0.30
LY09_sat	J	10-m wind speed at which surface drag coefficient is maximized	33	20 - 50

FIG. 1. A list of the input parameters perturbed in the MOAT analysis. The parameters are identified by a unique color and letter (A–J). Each input can take on one of four equally spaced values within the range given in the far-right column. For example, C7_{upwp} is assigned one of four possible values: 0.35, 0.5, 0.65, or 0.8.

$$n_{i+} = \begin{cases} 1, & \text{if } d_{ij} \ge 0\\ 0, & \text{otherwise} \end{cases}$$
 (8)

$$f_{j+} = \frac{1}{M} \sum_{i=1}^{M} n_{i+}.$$
 (9)

In this way, this study assesses three components of a parameter's sensitivity with respect to an output metric: the response of the output (μ_j^*) , the nonlinearity of the response (σ_i) , and the monotonicity, or direction, of the response (f_{i+}) .

The N=10 input parameters in Fig. 1 have been identified as potentially impactful in depicting the TC PBL. We choose the input perturbation ranges in Fig. 1 based on two factors: 1) previously established recommended values and 2) known stability considerations. For our study, we use M=15 paths, which is within the recommended range of $10 \le M \le 20$ (Covey et al. 2013; Morales et al. 2019) and results in 165 unique configurations of CAM6-CLUBBX. We run the MOAT analysis using the Sensitivity Analysis Library (SALib) package in Python3 (Herman and Usher 2017).

The day 10 zonal winds at the lowest model level (Figs. S3–S8) and the azimuthally averaged radial winds (Figs. S9–S14) for each unique configuration are provided in supplemental materials. All configurations produce cyclonic low-level flow and a realistic azimuthally averaged secondary circulation. However, some configurations exhibit early signs of numerical instability (i.e., high azimuthal variance in low-level wind speed), appearing most prominently in configurations with low vertical turbulent mixing. Though they present possible limitations in the utility of certain combinations of input parameter values, these configurations are still important to consider when assessing the sensitivity of model output to the perturbation of default CLUBBX parameter settings.

3. Results

a. Baseline CAM6-CLUBBX biases

We first establish a baseline for TC structure bias in CAM6-CLUBBX by comparing against both observations and a high-resolution, cloud-resolving model. This baseline analysis employs CLUBBX parameter settings (Fig. 1) largely based on those provided in the release version of CESM2 used for this study (see the acknowledgments). Figure 2 compares the vertical profiles of azimuthally averaged (Fig. 2a) tangential wind and (Fig. 2b) effective K_m in CAM6-CLUBBX to NOAA dropsonde observations and Cloud Model 1 (CM1, Bryan and Rotunno 2009; Bryan et al. 2017, see supplemental materials for details). CM1, which is a high-resolution, cloud-resolving model that uses nonhydrostatic dynamics, has been compared extensively to TC observations (e.g., Bryan 2012) and provides an additional benchmark for comparison to CAM6-CLUBBX.

While tangential wind profiles from the dropsondes and CM1 are maximized at or below 1000 m, the modeled CAM6-CLUBBX tangential wind profile continues to increase above 1000 m. Meanwhile, the profile of effective K_m in CAM6-CLUBBX is appreciably higher than CM1, implying that CAM6-CLUBBX produces more vertical turbulent mixing in the TC PBL. Figure 3a indicates that CAM6-CLUBBX also produces a TC PBL that is considerably warmer in the lowest several hundred meters compared to CM1 and observations. We note that the CM1 configuration shown here uses an SST that is about 3 K cooler than CAM6-CLUBBX, but the biases seen in Fig. 3a are likely not fully explained by differences in prescribed SSTs alone. The specific humidity profile in CAM6-CLUBBX is also too dry in the lowest several hundred meters (Fig. 3b).

These structural biases in Figs. 2 and 3 are also evident in the time series of height of maximum wind (Fig. 4a) and latent heat flux (LHF) fraction (Fig. 4b). As the TC matures, the height of maximum wind in CAM6-CLUBBX ranges from 2000 to 3000 m, which is 1000 to 2000 m greater than both the dropsonde composite and CM1. The LHF fraction, which is the ratio of surface LHF to total surface heat flux (latent + sensible), is also too high compared to CM1. We note that the LHF fraction is related to the Bowen ratio (B = SHF/LHF) as follows: $LH_{frac} = (1/B)[SHF/(B^2LHF + SHF)]$, so a high bias in LHF fraction implies a low bias in the Bowen ratio, with sensible heat flux (SHF) too low in comparison to LHF. This bias in LHF fraction occurs because the warm and dry biases in CAM6-CLUBBX suppress SHF and enhance LHF. In fact,

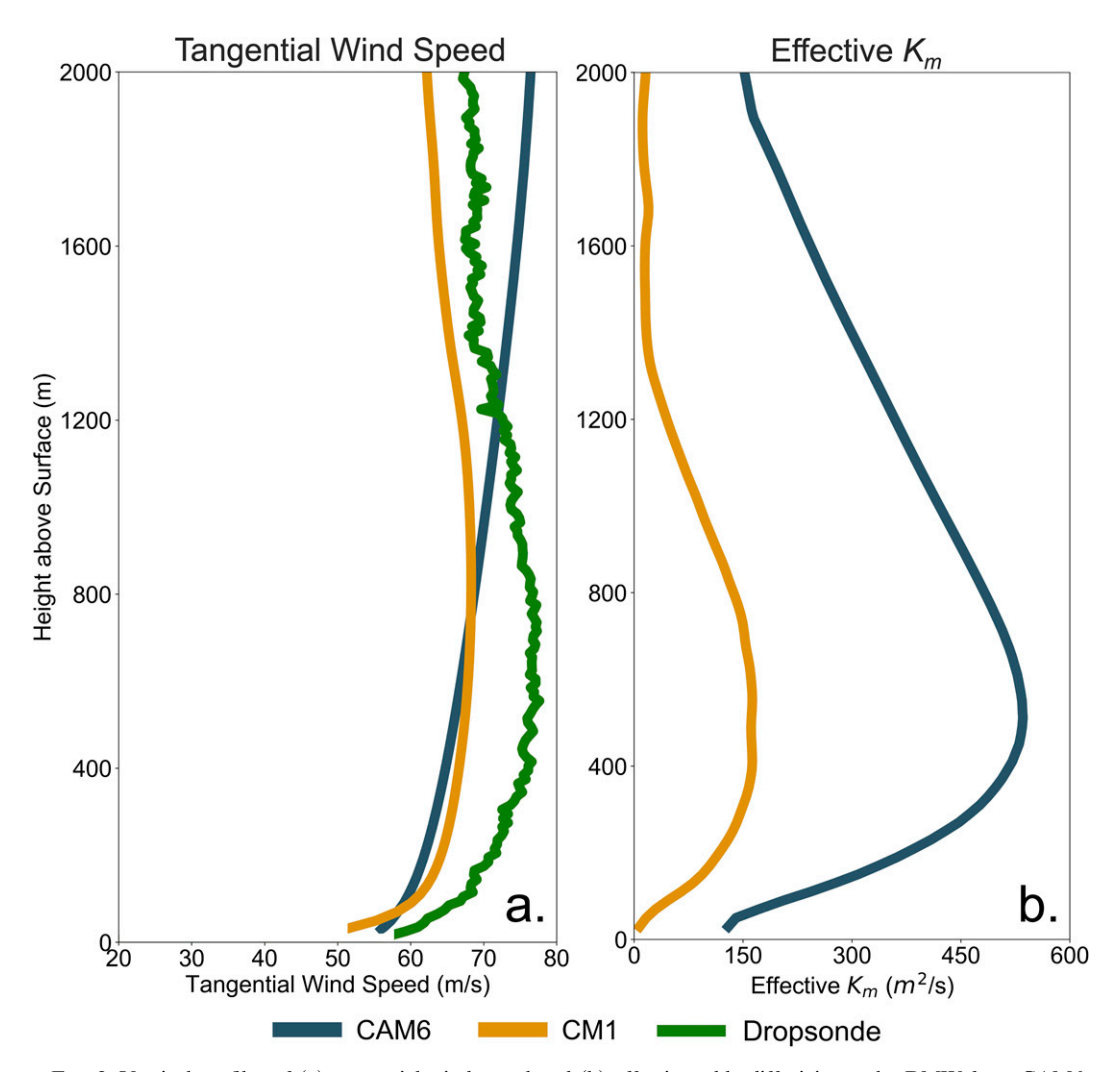


FIG. 2. Vertical profiles of (a) tangential wind speed and (b) effective eddy diffusivity at the RMW from CAM6-CLUBBX (dark blue) and CM1 (orange). In (a), the composite wind speed profile from NOAA dropsonde observations is shown in green. CAM6-CLUBBX profiles come from an idealized configuration using an average of 20 ensemble members over days 8, 10, and 12. The CM1 profile comes from an axisymmetric configuration at steady state.

CAM6-CLUBBX produces values of LH_{frac} in excess of 1, implying a negative SHF directed into the ocean. Accurate depictions of the jet maximum are critical because these winds can be advected downward in downdrafts and cause damage at the surface (Kepert 2001). Meanwhile, the LHF fraction affects the surface flux feedback, which is a major component of the moist static energy budget of mature TCs (Emanuel 1986; Wing et al. 2019). Therefore, biases in height of maximum wind and LHF fraction are important targets for model improvements.

b. MOAT analysis

To remove specific biases in CAM6-CLUBBX, we use the output from the MOAT analysis to identify input parameters that produce relatively large responses in a consistent direction. Therefore, we seek input parameters that produce a high value of μ_j^* , which is the average response of the output to

perturbing the input parameter value. Moreover, we seek input parameters that produce a consistent directional response, which means that increasing the parameter x_j should either frequently decrease or frequently increase the output y. Therefore, input parameters with a high value of μ_j^* should have a monotonicity, f_{j+} , close to 0 or 1. If an input parameter has a value of f_{j+} close to 0.5, it is unclear whether increasing the input would increase or decrease the model output, thus providing little value to developers. However, input parameters that meet both criteria listed above ensure that perturbing the parameter in a particular direction will reliably push the output metric in the direction necessary to improve simulations of TCs with CAM6-CLUBBX.

Figure 5 shows (Fig. 5a) μ_j^* and σ_j and (Fig. 5b) monotonicity f_{j+} for the N=10 input parameters with respect to the height of maximum tangential wind. In this and subsequent figures, each input parameter is assigned a unique color and letter ID (Fig. 1). The terms μ_j^* and σ_j for each input are

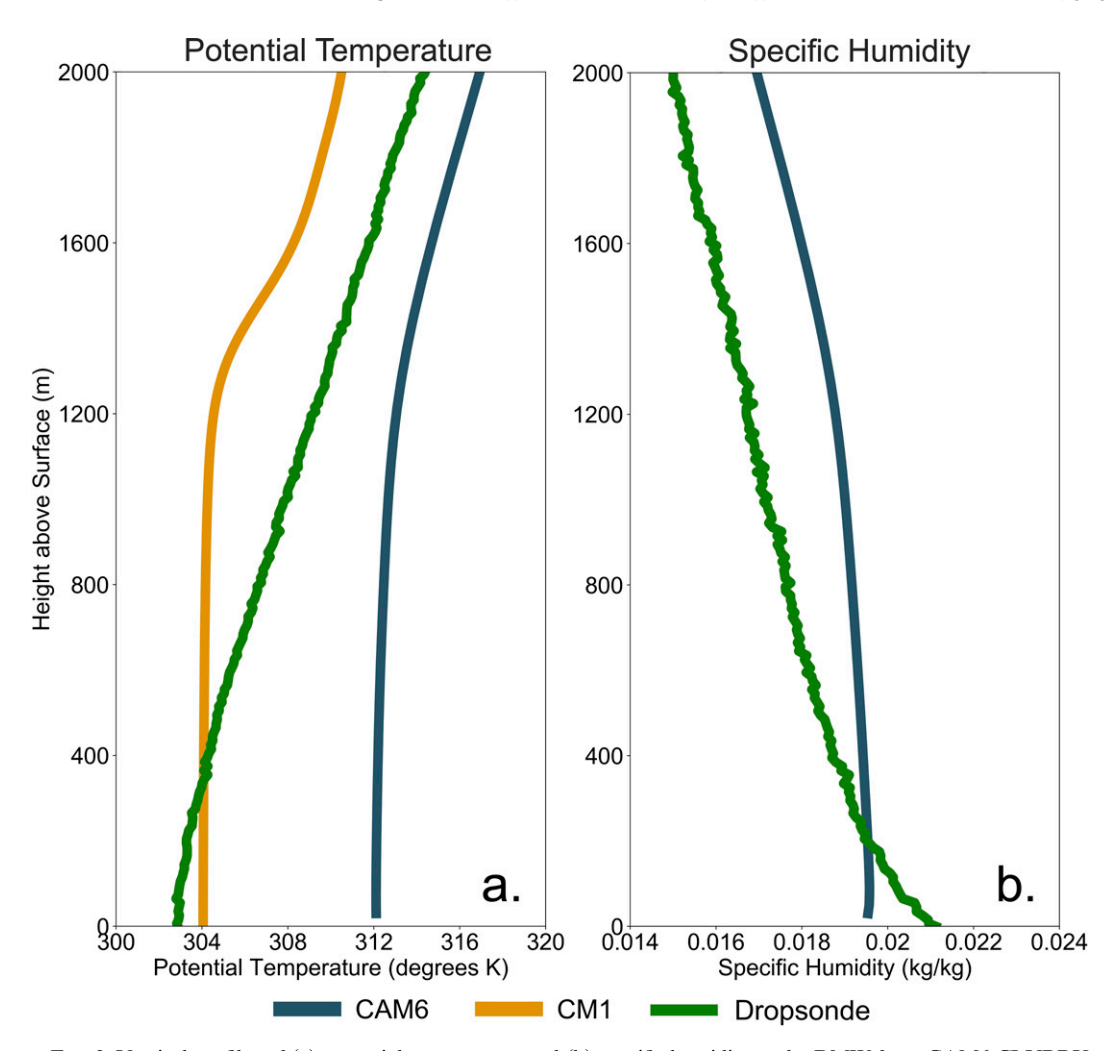


FIG. 3. Vertical profiles of (a) potential temperature and (b) specific humidity at the RMW from CAM6-CLUBBX (dark blue) and CM1 [orange, (a) only]. The composite temperature and moisture profiles from NOAA dropsonde observations are shown in green. CAM6-CLUBBX profiles come from an idealized configuration using an average of 20 ensemble members over days 8, 10, and 12. The CM1 profile comes from an axisymmetric configuration at steady state.

normalized such that they fall between 0 (least response or least nonlinearity) and 100 (greatest response or greatest nonlinearity). Therefore, input parameters located near the right edge of the left panel (μ_i^* values closer to 100) produce the greatest response with respect to height of maximum wind, while those near the upper edge (σ_i values closer to 100) produce the greatest nonlinear response. For the height of maximum wind, the input parameters are arranged such that those producing a large μ_i^* also produce a large σ_i , signaling a large average response but also high variability in the response based on the choice of background state. This implies that these high-response input parameters may derive their sensitivities from nonlinear interactions between different aspects of the PBL, as well as interactions with other components of the climate system. While high variability in the response is not ideal for targeted perturbations to input parameters, a high or low value of f_{i+} can still give model developers confidence that the direction of the response is at least consistent.

The vertical axis of the right panel is f_{j+} , the frequency with which increasing the input increases the height of maximum wind. The input's unique letter ID is located on the horizontal axis of the right panel. If an input parameter is located at the bottom (f_{j+} close to 0) or top of the plot in the right panel (f_{j+} close to 1), increasing the input consistently decreases or increases, respectively, the height of maximum wind. Meanwhile, an input parameter located toward the middle of the plot (f_{j+} close to 0.5) provides an inconsistent directional response. Figure 6 similarly shows (Fig. 6a) μ_j^* and σ_j and (Fig. 6b) f_{j+} with respect to the LHF fraction.

We also broaden our analysis and assess the sensitivity of other aspects of TC structure to the N=10 input parameters. In Fig. 7, each input parameter on the vertical axis is ranked according to the magnitude of the response (μ_j^*) of each output metric on the horizontal axis. For example, height of maximum wind is most sensitive to C_invrs_tau_sfc (highest μ_j^*) and least sensitive to C4 (lowest μ_j^*). Table 2 provides a key

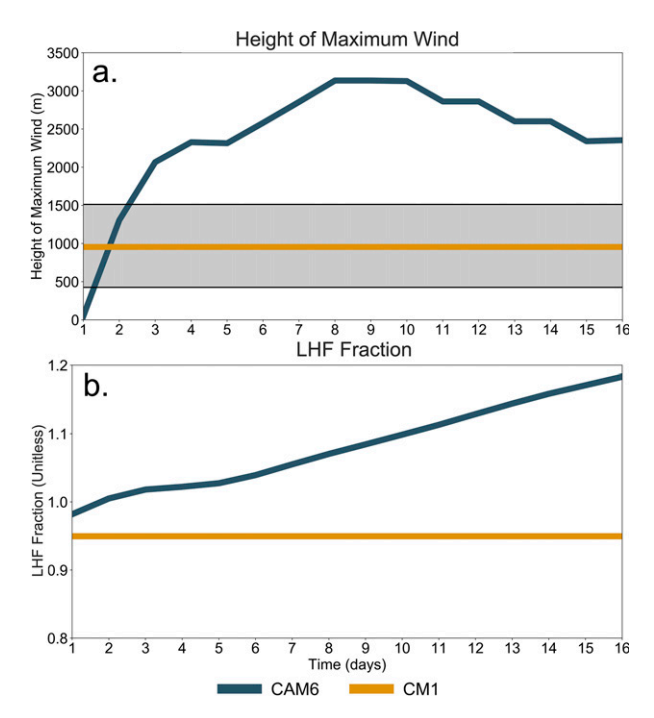


FIG. 4. Time series of (a) the height of maximum wind and (b) latent heat flux (LHF) fraction from CAM6-CLUBBX (dark blue) and CM1 (orange). In (a), gray shading denotes the interquartile range of NOAA dropsonde observations of height of maximum wind. CAM6-CLUBBX time series come from an idealized configuration using an average of 20 ensemble members over days 8, 10, and 12. The CM1 value in (a) comes from an axisymmetric configuration at steady state, while the value in (b) comes from a full 3D configuration at steady state (see supplemental material).

for the output metric abbreviations, while the supplemental materials detail how each output is calculated. Figure 8 highlights similar rankings with respect to σ_j , while the grid in Fig. 9 shows f_{j+} for each input–output pair.

Figures 7–9 illustrate the variability in an input parameter's sensitivity across the various TC structural outputs. Though it is not the goal of this study, it is difficult to definitively identify one particular input parameter that produces the most sensitivity across all outputs. Therefore, we choose to isolate a handful of input parameters that merit additional analysis. We reiterate that we are not specifically advocating for these input parameters as the best candidates to change in CAM6-CLUBBX. These input parameters fit the aforementioned criteria (e.g., strong, consistent directional responses) across a broad spectrum of TC structural metrics in Figs. 7–9. Three input parameters of note are C14 (A, dark green in Fig. 5), C7_{upwp} (C, dark blue), and C_invrs_tau_sfc (G, pink).

Notably, all three input parameters are directly tied to CLUBBX's formulation of vertical momentum flux and effective eddy diffusivity. C14 is a coefficient attached to a damping term in the budgets of the horizontal variance terms u'^2 and $\overline{v'^2}$. Therefore, an increase in this term is expected to reduce TKE in the TC PBL. $C7_{\rm upwp}$ is a coefficient in Eq. (4) that offsets the turbulent production of momentum flux due

to updrafts and downdrafts. Increasing this term would therefore result in a decrease in the magnitude of momentum flux and a decrease in effective eddy diffusivity. C_invrs_tau_sfc is the constant coefficient $C_{\rm sfc}$ in Eq. (6) that governs the degree of turbulent eddy dissipation (i.e., the breakup of larger turbulent eddies into smaller turbulent eddies) due to surface friction. Increasing this term would result in an increase in $1/\tau$ and a decrease in turbulent length scale L near the surface. The influence of $C7_{\rm upwp}$ and C_invrs_tau_sfc is made clear by simplifying Eq. (4) by assuming that the turbulent production of $\overline{u'w'}$ by updrafts and downdrafts (term 3) and the return-to-isotropy adjustment (term 6) dominate. After rearranging, Eq. (4) reduces to the diagnostic downgradient diffusion approximation:

$$\overline{u'w'} = -K_{\text{approx}} \frac{\partial \overline{u}}{\partial z},\tag{10}$$

$$K_{\text{approx}} = \frac{\left(1 - C_{7upwp}\right)\tau \overline{w'^2}}{C_6}.$$
 (11)

Therefore, increasing $C7_{upwp}$ or decreasing τ (by increasing $C_{invrs_tau_sfc}$) will act to reduce vertical eddy diffusivity and associated turbulent mixing.

Though sensitivities vary, inputs that produce high sensitivity with respect to height of maximum wind and LHF fraction also produce high sensitivity for other output metrics. For example, C14 falls within the top half of the μ_j^* rankings for 10 out of 14 output metrics evaluated, while both C7_{upwp} and C_invrs_tau_sfc fall within the top half for 13 out of 14 output metrics evaluated. Moreover, outputs that are physically related have similar μ_j^* rankings. For example, the rankings for minimum surface pressure and maximum 10-m wind speed are nearly identical, while the rankings for LHF fraction are similar to those for 100-m potential temperature and specific humidity.

In general, C14, C7 $_{\rm upwp}$, and C_invrs_tau_sfc also produce highly nonlinear responses for most output metrics (Fig. 8). C14 is in the top half of the σ rankings for all 14 output metrics. $C7_{upwp}$ is in the top half of σ rankings for 12 of 14 output metrics, while C_invrs_tau_sfc is in the top half for 10 of 14 output metrics. All three of these input parameters have direct impacts on vertical turbulent mixing in the PBL. This modulation of turbulent mixing can influence the distribution of heat and moisture in the PBL, which in turn affects other aspects of the model physics, including convection and microphysics. Therefore, the high values of σ may be explained by the nonlinear interactions between turbulence, convection, and precipitation processes. However, we caution that the unraveling of nonlinear physical interactions within the TC PBL is beyond the scope of this study. Nonetheless, future work should examine these nonlinearities further.

As with height of maximum wind and LHF fraction, C14, C7_{upwp}, and C_invrs_tau_sfc stand out in Fig. 9 for widely producing a consistent directional response, with f_{j+} values greater than 0.7 or less than 0.3 for most output metrics. This indicates that these three inputs may be good targets for improvement in output metrics. Though these input

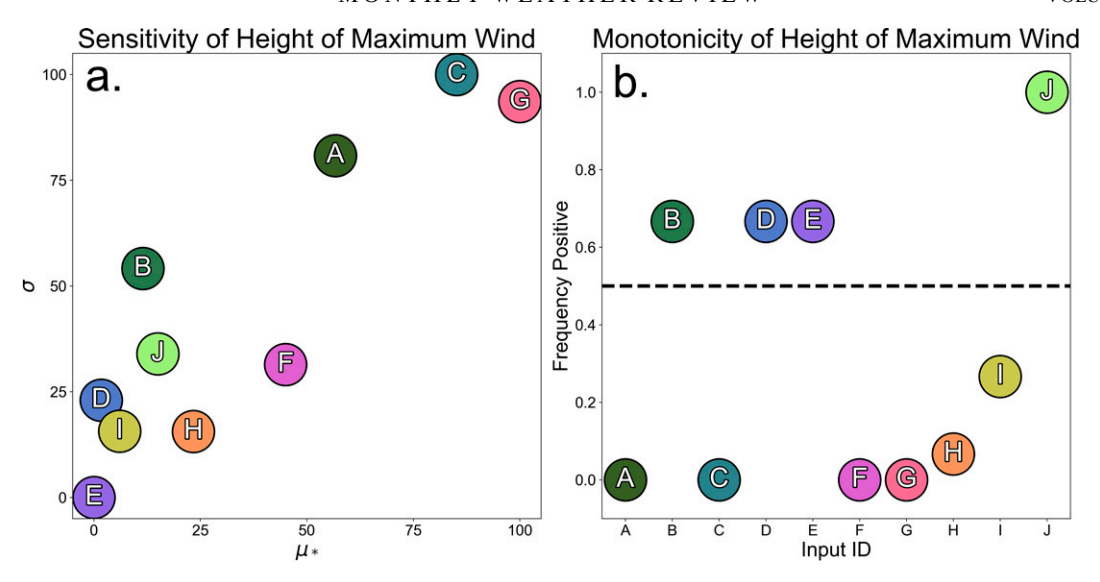


FIG. 5. (a) The sensitivity of the height of maximum wind to perturbations of the N=10 input parameters. Figure 1 lists the colors and letters corresponding to each input. The term μ_j^* represents the average influence of changing the input on the height of maximum wind, while σ_j represents the nonlinear effects of the input on the height of maximum wind; μ_j^* and σ_j are standardized so that $\mu_j^* = \left(\mu_j^* - \mu_{\min}^*\right) / \left(\mu_{\max}^* - \mu_{\min}^*\right) \times 100$ and $\sigma_j = (\sigma_j - \sigma_{\min}) / (\sigma_{\max} - \sigma_{\min}) \times 100$. (b) The frequency (f_{j+}) of an increase in height of maximum wind fraction given an increase in the input parameter. Height of maximum wind is averaged over days 8, 10, and 12.

parameters produce responses that are more variable due to nonlinear effects (Fig. 8), there is greater confidence that the responses are still in a consistent direction. Furthermore, outputs that are physically related again have similar degrees of consistency in directional response. For example, inputs that

frequently decrease LHF fraction frequently increase 100-m specific humidity and decrease 100-m potential temperature. This provides evidence that the MOAT analysis adequately captures the expected physical relationships between output metrics when calculating sensitivities.

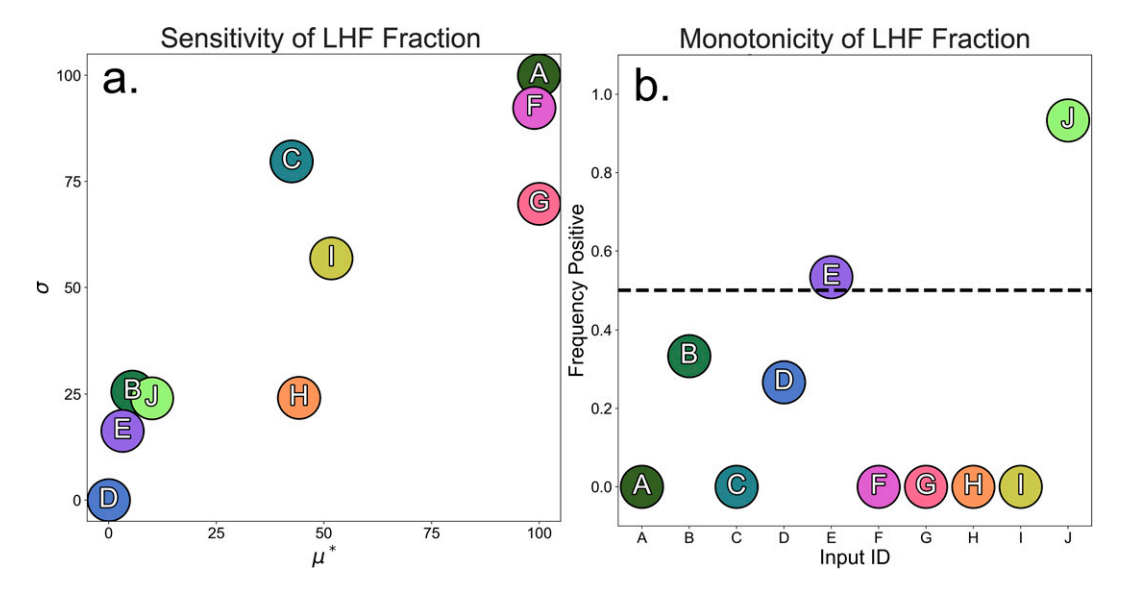


Fig. 6. (a) The sensitivity of the latent heat flux (LHF) fraction to perturbations of the N=10 input parameters. Figure 1 lists the colors and letters corresponding to each input. The term μ_j^* represents the average influence of changing the input on the LHF fraction, while σ_j represents the nonlinear effects of the input on the LHF fraction; μ_j^* and σ_j are standardized so that $\mu_j^* = \left(\mu_j^* - \mu_{\min}^*\right) / \left(\mu_{\max}^* - \mu_{\min}^*\right) \times 100$ and $\sigma_j = (\sigma_j - \sigma_{\min}) / (\sigma_{\max} - \sigma_{\min}) \times 100$. (b) The frequency (f_{j+}) of an increase in LHF fraction given an increase in the input parameter. LHF fraction is averaged over days 8, 10, and 12.

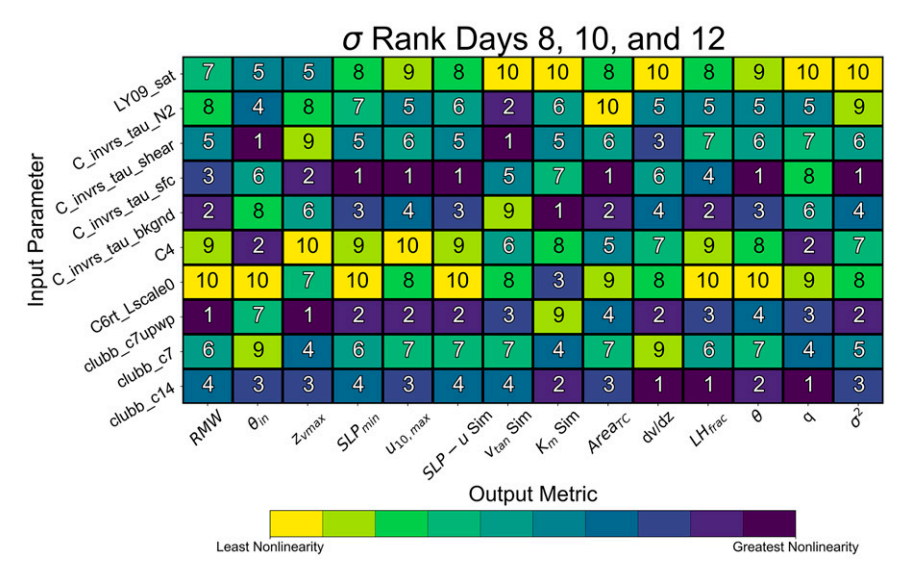


FIG. 8. For each output metric, a ranking of the input parameters based on the value of σ_j (rankings from 1 to 10, highest to lowest). Higher rankings (darker colors) imply that perturbing the input parameter produces greater nonlinear effects with respect to the output metric, while lower rankings (brighter colors) imply that perturbing the input parameter produces smaller nonlinear effects with respect to the output metric. Table 2 provides a key for the output metric abbreviations.

CLUBBX (Figs. 2–4) in order to specifically reduce biases in height of maximum wind and LHF fraction. We choose a simple case in which a single input parameter is gradually changed over 10 configurations of CAM6-CLUBBX. In practice, model improvements would seek to reduce biases in a

wider range of TC structural characteristics, likely employing multiple input parameter perturbations. However, these experiments are meant to provide a simplified illustration of the physical processes governing the sensitivities seen in the MOAT analysis.

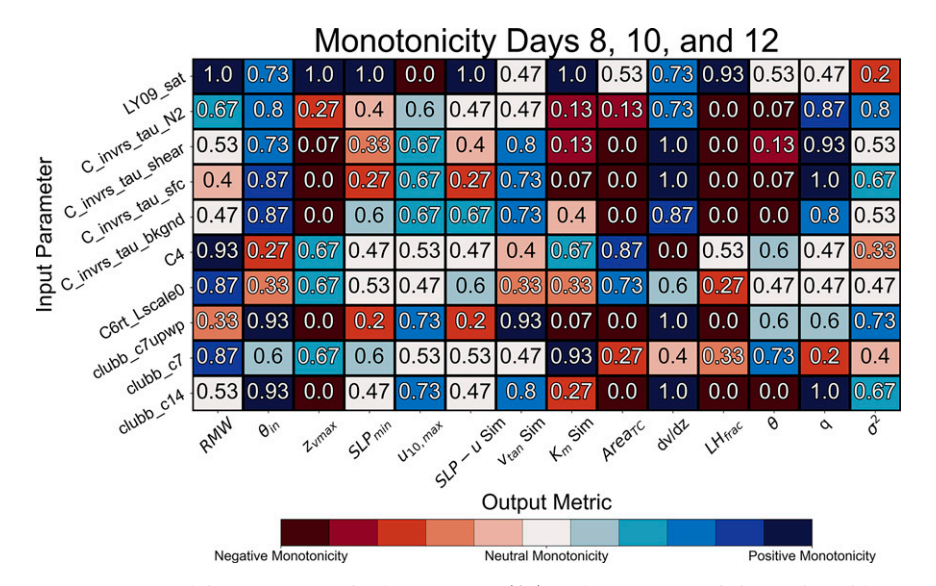


FIG. 9. For each input—output pair, the frequency (f_{j+}) of the output metric increasing with an increase in the input parameter. Values greater than 0.5 (blues) imply that increasing the input parameter more often increases the output metric, while values lower than 0.5 (reds) imply that increasing the input parameter more often decreases the output metric. Dark blues imply a consistent increase, while dark reds imply a consistent decrease. Table 2 provides a key for the output metric abbreviations.

Since CAM6-CLUBBX overestimates both the height of maximum wind and LHF fraction, we seek a parameter with relatively high μ_i^* and relatively low f_{i+} . Therefore, we choose to target one of the four input parameters identified above. We specifically highlight the impact of perturbing C_invrs_tau_shear, as it produces modest sensitivities over most output metrics but is also expected to have impacts confined to high-shear areas such as TCs. C7_{upwp} is similarly tied to a vertical wind shear term in Eq. (4), so its impacts are also expected to be largely isolated to TCs. However, unlike C_invrs_tau_shear, C7_{upwp} only indirectly influences fluxes of scalars like θ and q, which is consistent with the lower sensitivity of C7_{upwp} with respect to low-level thermodynamic quantities (Fig. 7). While increasing C_invrs_tau_shear provides one potential pathway to reducing CAM6-CLUBBX bias, a formal endorsement of an updated CAM6-CLUBBX configuration suitable for the global climate is beyond the scope of this study. A repeat of the following analysis with C_invrs_tau_sfc (Fig. S15) and C7_{upwp} (Fig. S16) indicates that these input parameters provide additional pathways toward reducing model biases.

Figure 10 shows the progression of the ensemble-averaged (k = 20) (Fig. 10a) height of maximum wind and (Fig. 10b) the LHF fraction as C_invrs_tau_shear is gradually increased from 0.02 to 0.20, with all else constant, in one particular model state (the baseline combination of input parameters from Figs. 2-4). All 10 configurations produce physically plausible ensemble-averaged TC structures (see Figs. S17 and S18). For reference, the brown line denotes the value of C_invrs_tau_shear used in the baseline CAM6-CLUBBX configuration in Fig. 4. Figure 10 indicates that increasing C invrs tau shear decreases both the height of maximum wind and the LHF fraction, as seen in the progression from brown to pink lines. Both are consistent with the predicted outcomes from the MOAT analysis in Figs. 5 and 6. Moreover, the time series of both outputs gradually approach observations (gray shading) and/or CM1 (orange). In this example, the MOAT analysis objectively identifies a high-sensitivity input parameter, like C_invrs_tau_shear, that provides a pathway to reducing model bias in height of maximum wind.

Increasing C_invrs_tau_shear monotonically reduces the turbulent length scale (Fig. 11a) and effective eddy diffusivity K_m (Fig. 11b) throughout the TC PBL at the RMW. The reduction in effective K_m produces more realistic values of these quantities compared to observations from intense TCs (e.g., Zhang et al. 2011). Figure 12 provides a broader perspective by showing the radial cross section of a given output's response to increasing C_invrs_tau_shear. At each radius and vertical level, Fig. 12 quantifies the response by linearly regressing the output metric on C_invrs_tau_shear and calculating the slope of the best-fit line using ordinary least squares (OLS). For example, reds in Fig. 12a imply that increasing C_invrs_tau_shear decreases the tangential wind at that location, while blues imply that increasing C_invrs_tau_shear increases the tangential wind at that location. As C_invrs_ tau_shear increases, the height of maximum tangential wind decreases from around 3000 m to 1000 m. The hatching in Fig. 12 denotes radius-level pairs at which the Spearman rank

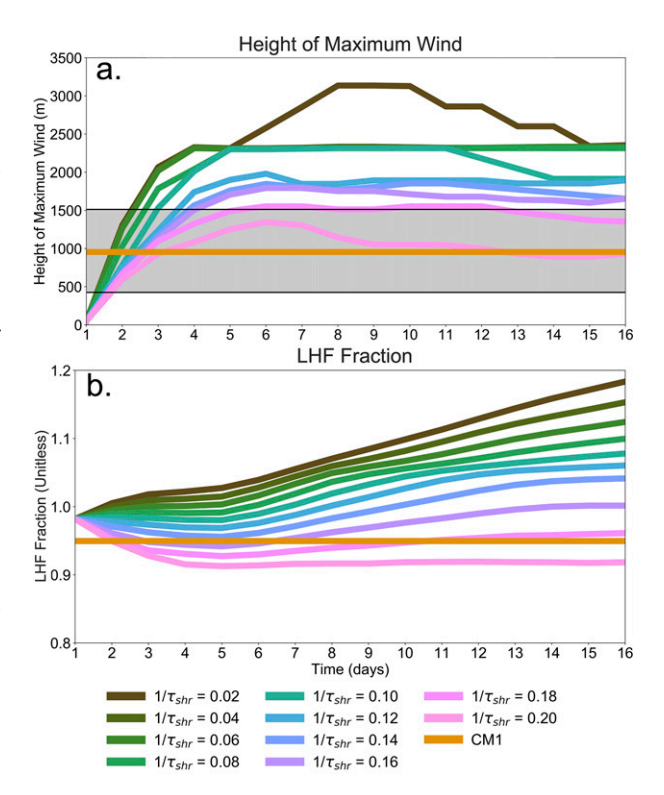


FIG. 10. Time series of (a) height of maximum wind and (b) latent heat flux (LHF) fraction from idealized configurations of CAM6-CLUBBX with varying values of C_invrs_tau_shear. Darker lines denote configurations with lower C_invrs_tau_shear, while brighter colors denote configurations with higher C_invrs_tau_shear. The steady-state values of height of maximum wind and latent flux fraction from an axisymmetric configuration in (a) and full 3D CM1 configuration in (b) are in gold. Gray shading in (a) denotes the interquartile range of NOAA dropsonde observations. CAM6-CLUBBX time series are averaged over 20 ensemble members.

correlation (Wilks 2011) between the output and C_invrs_tau_shear has a magnitude greater than 0.8, which implies a highly monotonic relationship. The lack of hatching in some locations indicates that the sensitivity of C_invrs_tau_shear is not purely monotonic everywhere, likely due to nonlinear interactions between the the model's dynamical core, turbulence, microphysics, and convective parameterizations that merit future research.

Figures 12e and 12f also highlight a decrease in the turbulent length scale L and effective K_m due to an increase in $C_{invrs_tau_shear}$. Increasing $C_{invrs_tau_shear}$ adds weight to the wind shear dissipation term in Eq. (6), representing increased dissipation associated with the high-shear environment of the lower TC PBL. In CLUBBX, this process decreases L, which physically represents the shear-induced distortion of larger turbulent eddies into smaller eddies (e.g., Mauritsen and Enger 2008). The decrease in L and effective K_m keeps the turbulent mixing confined to the lowest several hundred meters. This is evident in Fig. 12d, which shows that the magnitude of the zonal component of momentum flux $(\overline{u'w'})$ decreases above 1000 m, but increases below 1000 m,

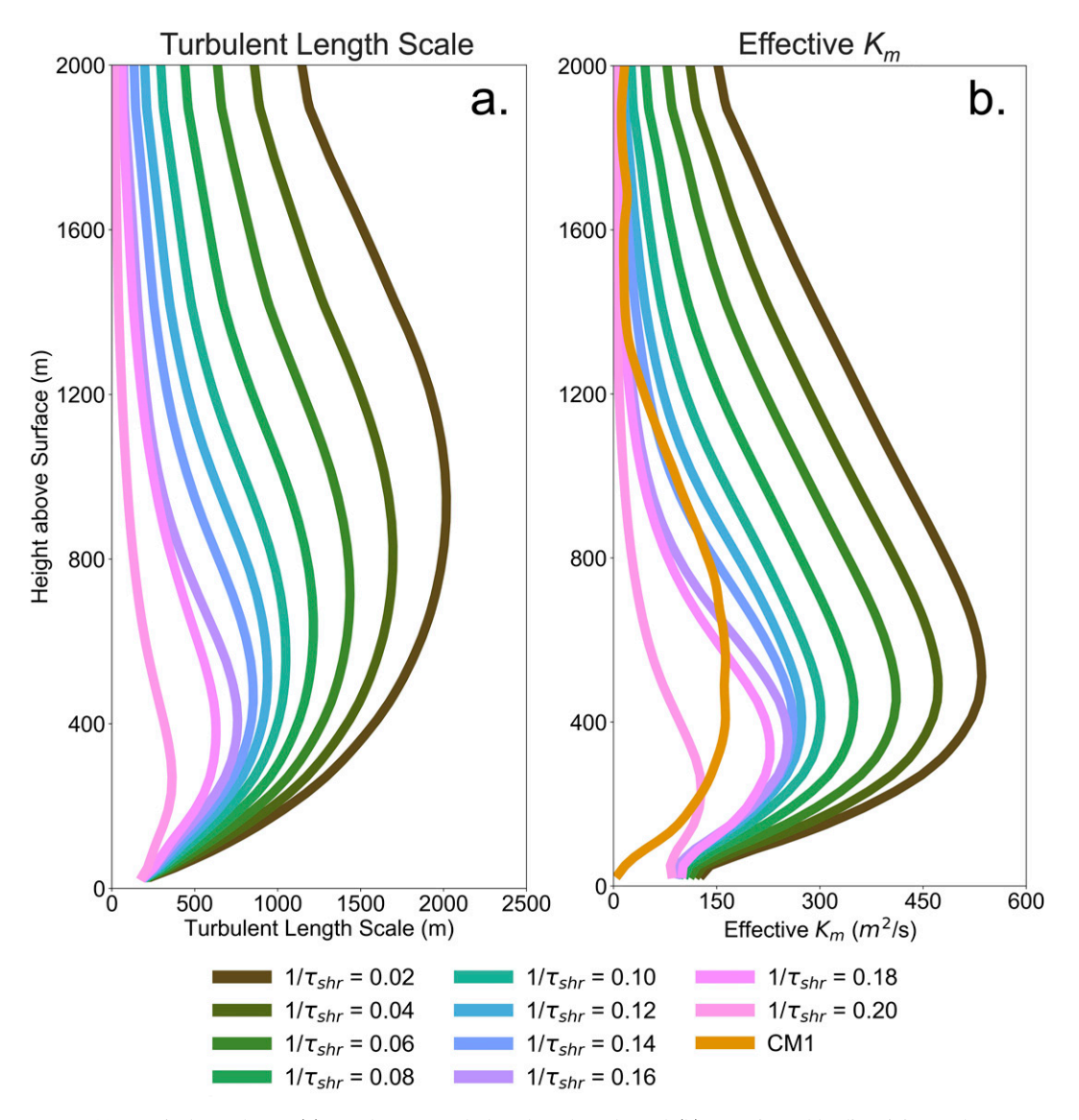


FIG. 11. Vertical profiles of (a) steady-state turbulent length scale and (b) effective eddy diffusivity at the RMW from idealized configurations of CAM6-CLUBBX with varying values of C_invrs_tau_shear. Darker profiles denote configurations with lower C_invrs_tau_shear, while brighter colors denote configurations with higher C_invrs_tau_shear. Profiles from an axisymmetric CM1 configuration are in orange. CAM6-CLUBBX profiles are averaged over 20 ensemble members at days 8, 10, and 12.

with an increase in C_invrs_tau_shear. Physically, the turbulent eddies are still maintained in the lowest several hundred meters due to increased vertical wind shear. However, these turbulent eddies remain small, and turbulence is not able to diffuse upward.

Increased dissipation of turbulent eddies, and the resulting reduction in effective K_m seen in Fig. 12f, thus provides a mechanism for reducing the height of maximum wind, which has been shown to be proportional to K_m (Kepert 2001; Kepert and Wang 2001). Therefore, a modification that decreases effective K_m in CAM6-CLUBBX is expected to decrease the height of maximum wind, which is consistent with the findings of Kepert (2012), who found that PBL

schemes that produced lower eddy diffusivity also produced a lower height of maximum wind in a diagnostic TC PBL model (Kepert and Wang 2001). In addition, Bryan (2012) found that reducing the vertical turbulent length scale in CM1 reduced the modeled height of maximum wind, while Gopalakrishnan et al. (2013) found that reducing K_m in HWRF reduced the inflow depth in modeled TCs. Most recently, Gopalakrishnan et al. (2021) applied different PBL schemes to TC forecasts from the next-generation HAFS model and found that schemes with lower eddy diffusivity produced lower heights of maximum wind.

Figures 12b and 12c also highlight how increasing C_invrs_tau_shear affects the TC secondary circulation. For example,

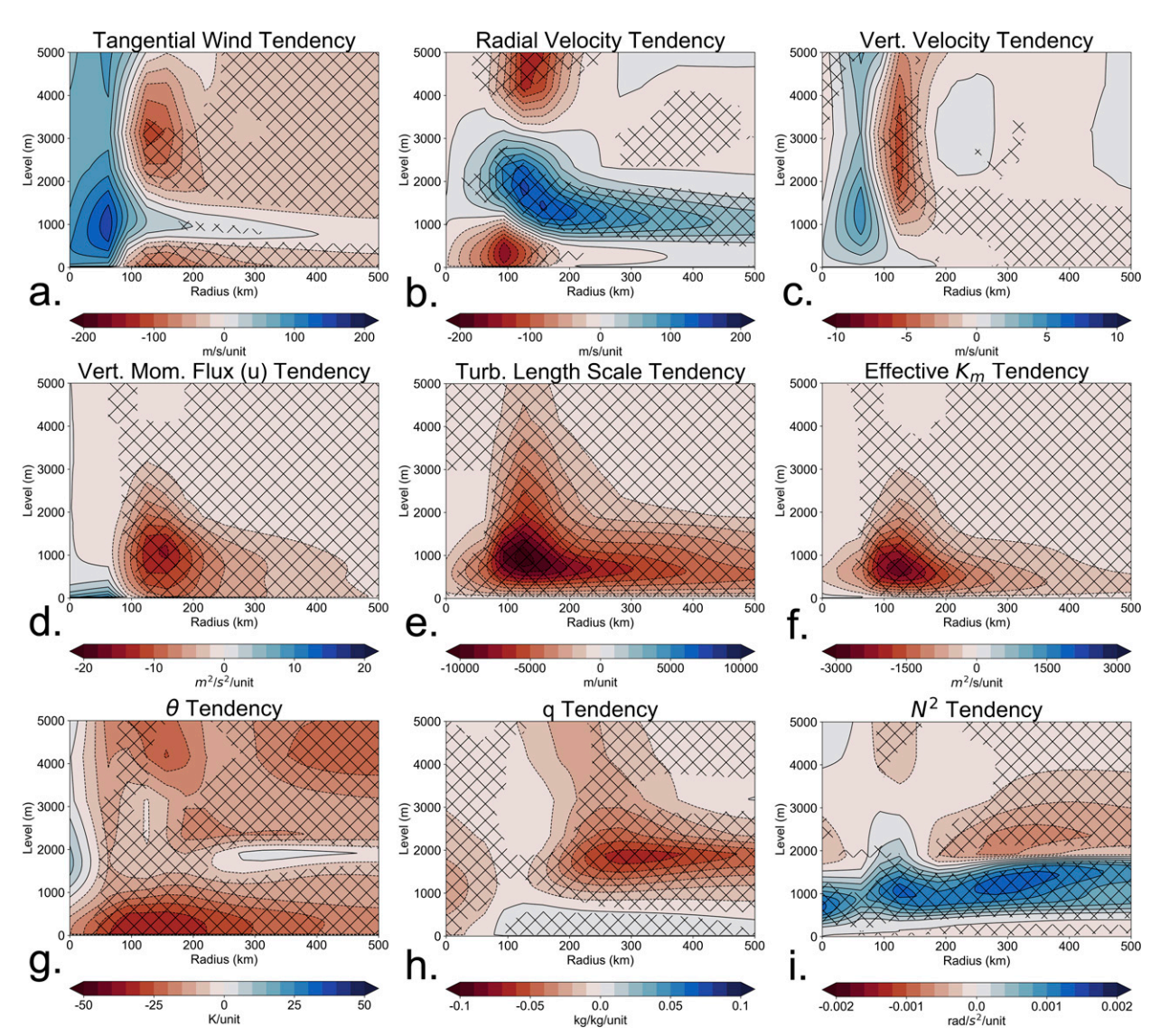


FIG. 12. The response of azimuthally averaged CAM6-CLUBBX (a)—(c) wind, (d)—(f) turbulence, and (g)—(i) thermodynamic fields given an increase in C_invrs_tau_shear. For a particular radius and vertical level, the response is calculated as the slope of the ordinary least squares (OLS) linear fit between the output and the value of C_invrs_tau_shear. Reds imply a decrease in the output as C_invrs_tau_shear increases, while blues imply an increase in the output as C_invrs_tau_shear increases. Profiles are averaged over 20 ensemble members at days 8, 10, and 12. Hatching denotes radius-level pairs at which the Spearman rank correlation between the output and C_invrs_tau_shear has a magnitude greater than 0.8.

Fig. 12b shows an appreciable increase in radial inflow below 1000 m. Here, radial wind directed inward toward the TC center is assigned a negative sign. As C_invrs_tau_shear increases, reduced vertical mixing effectively compresses, and moves inward, the couplet of inflow below the jet and outflow above (Gopalakrishnan et al. 2013; Kepert 2001; Kepert and Wang 2001). Such a response helps explain the increased inflow below 1000 m and the increased outflow above. Moreover, Gopalakrishnan et al. (2013) found that a shallower, less diffusive TC PBL caused a strengthening of radial inflow below jet height due to an increase in frictional forces. Gopalakrishnan et al. (2021) found a similar relationship in

HAFS, specifically showing that a reduction in K_m in the lower TC PBL enhanced radial inflow. These findings are also consistent with Bryan (2012), who found that reducing the vertical turbulent length scale l_v increased the surface inflow angle in an axisymmetric configuration of CM1. In CAM6-CLUBBX, we find an increase in surface inflow angle, indicating a strengthened inflow component, when we reduce vertical turbulent mixing by increasing C_invrs_tau_shear (Fig. 9). Therefore, the response in radial inflow is likely a combination of both shifting the inflow-outflow couplet downward and inward and strengthening the near-surface inflow due to frictional effects.

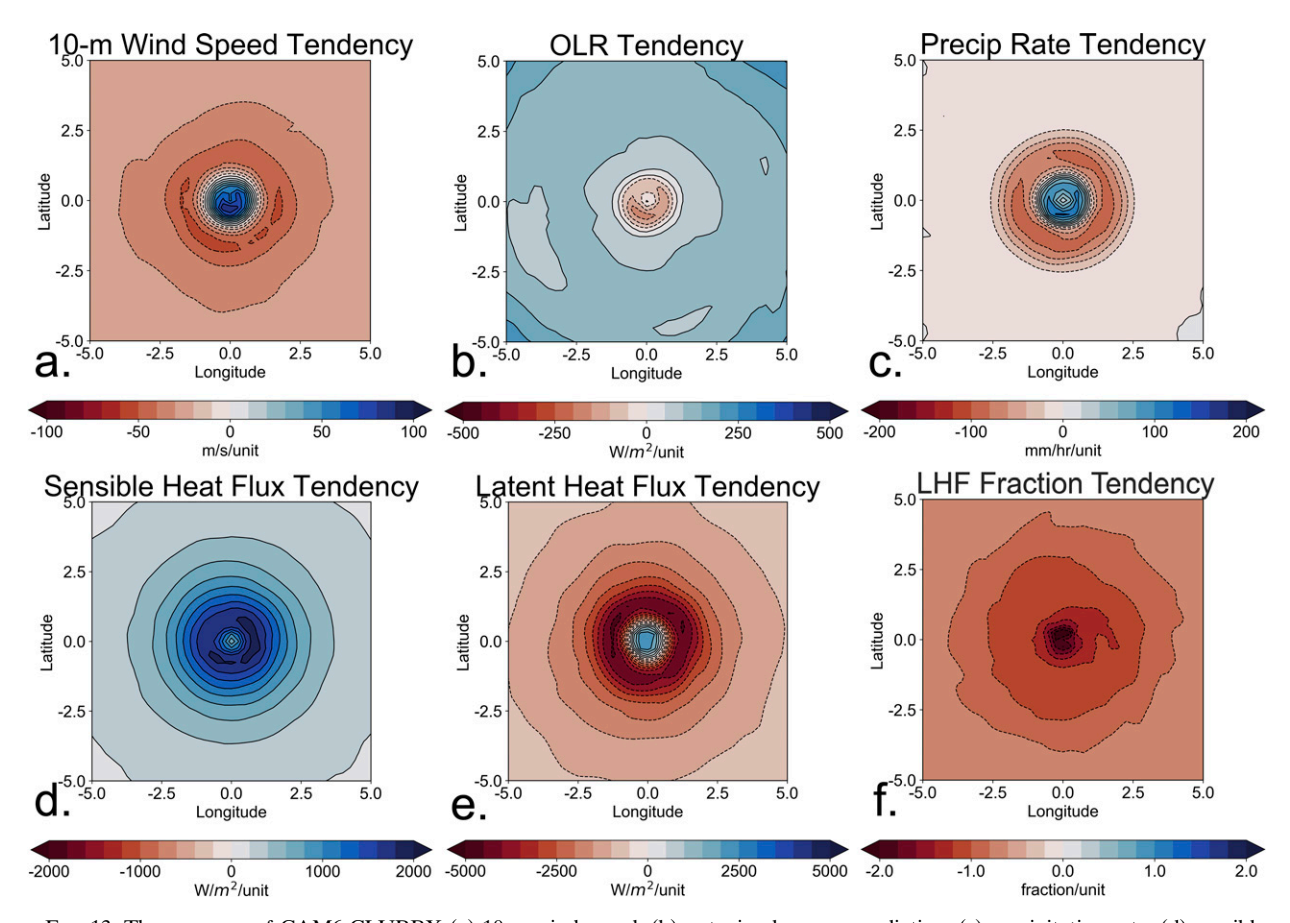


FIG. 13. The response of CAM6-CLUBBX (a) 10-m wind speed, (b) outgoing longwave radiation, (c) precipitation rate, (d) sensible heat flux (SHF), (e) latent heat flux (LHF), and (f) LHF fraction given an increase in C_invrs_tau_shear. For a particular latitude–longitude pair, the response is calculated as the slope of the ordinary least squares (OLS) linear fit between the output and the value of C_invrs_tau_shear. Reds imply a decrease in the output as C_invrs_tau_shear increases, while blues imply an increase in the output as C_invrs_tau_shear increases. Profiles are averaged over 20 ensemble members at days 8, 10, and 12.

Figures 12a and 12c also highlight a notable inward shift in the peak tangential and vertical wind speeds toward the center of the TC, indicating a contraction of the eyewall. This is consistent with Fig. 13, which similarly shows the change in the 2D plan view of the modeled TC as C_invrs_tau_shear increases. From Figs. 13a-c, it is clear that 10-m wind speed and precipitation rate increase and outgoing longwave radiation (OLR) decreases at lower radii. The apparent movement of the eyewall toward the center of the modeled TC compares favorably to the findings of Gopalakrishnan et al. (2013) and Bu et al. (2017), who found that reducing the degree of vertical turbulent mixing in the TC PBL in HWRF produced an inward movement of the eyewall. This is also consistent with our finding that increasing C_invrs_tau_shear decreases TC area over all M = 15 MOAT paths (Fig. 9). However, we note that while the eyewall updrafts shift inward, the peak vertical velocities appear to weaken as C_invrs_tau_shear increases. This contradicts past studies that found a strengthening of eyewall updrafts with decreased turbulent mixing (e.g., Gopalakrishnan et al. 2013), further underscoring the need to explore the nonlinear interactions between parameterized

turbulence and convection in CAM6-CLUBBX. However, it is important to note that most prior studies have examined higher-resolution simulations (~5 versus ~25 km in CAM6-CLUBBX). Therefore, future analysis should focus on quantities like parameterized convective mass flux instead of model-resolved vertical velocity, which likely does not fully characterize the modeled convective fluxes in CAM6-CLUBBX.

Figure 14 demonstrates that increasing C_invrs_tau_shear monotonically decreases 100-m potential temperature (Fig. 14a) and increases 100-m specific humidity (Fig. 14b) at the RMW, as anticipated by the MOAT analysis (Fig. 9). The near-surface cooling and moistening seen in Fig. 14 at the RMW are also prevalent over a large swath of the TC's lower levels (Figs. 12g,h). As a result of cooler and moister air just above the sea surface due to increasing C_invrs_tau_shear, surface SHF increases and LHF decreases throughout the TC (Figs. 13d,e). Therefore, LHF fraction is also reduced (Fig. 13f), which is again consistent with the MOAT analysis.

The low-level cooling that peaks 100 km away from the TC center is likely partially explained by an increase in evaporative cooling from precipitation that has shifted toward those

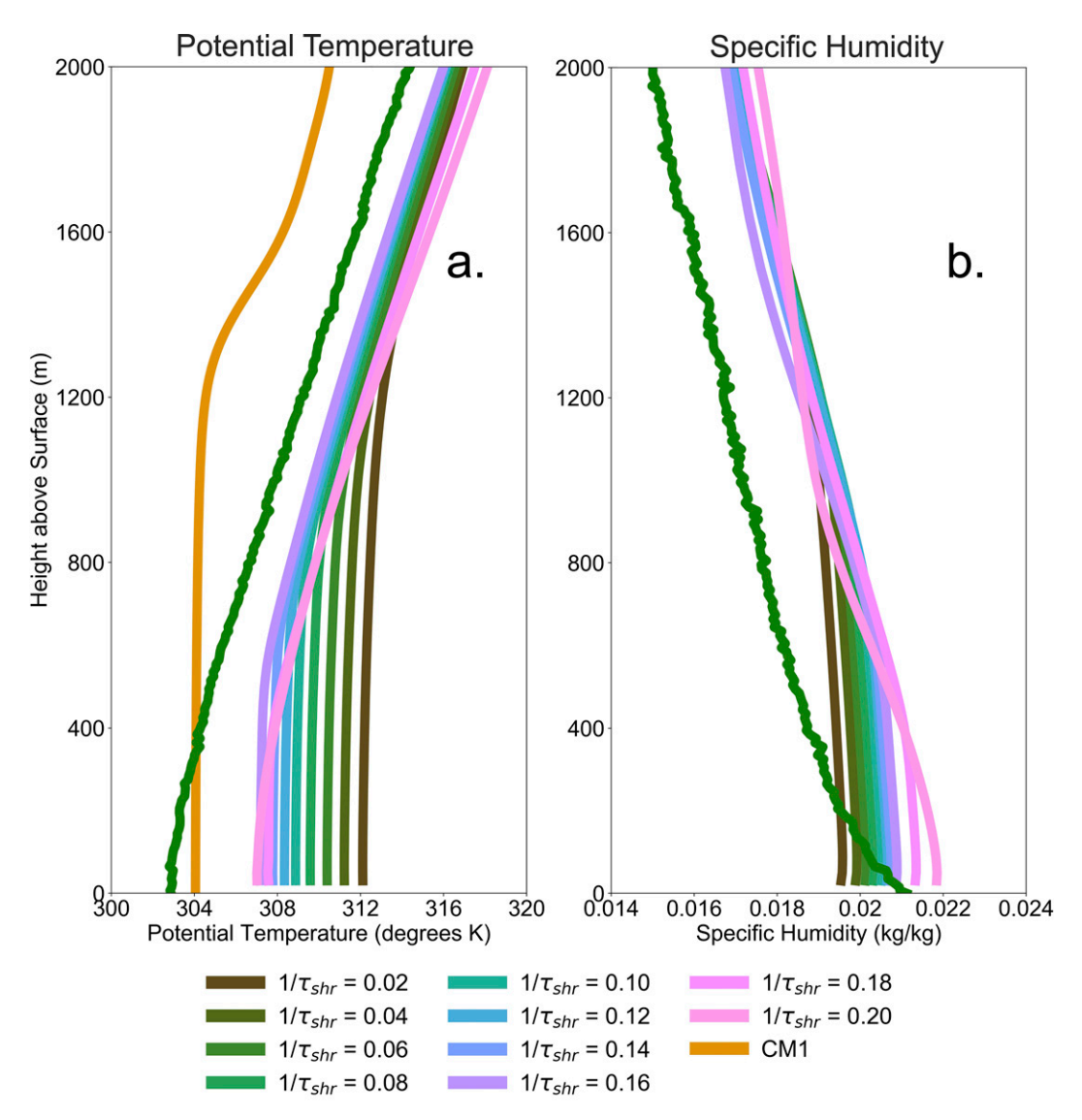


FIG. 14. Vertical profiles of steady-state (a) potential temperature and (b) specific humidity at the RMW from idealized configurations of CAM6-CLUBBX with varying values of C_invrs_tau_shear. Darker profiles denote configurations with lower C_invrs_tau_shear, while brighter colors denote configurations with higher C_invrs_tau_shear. The vertical profile from an axisymmetric CM1 configuration is in orange in (a), while the vertical profiles from composite NOAA dropsonde observations are in green in (a) and (b). CAM6-CLUBBX profiles are averaged over 20 ensemble members at days 8, 10, and 12.

radii (Fig. 13c). Also, Kepert et al. (2016) demonstrated that increased inflow near the RMW produced a cooling tendency in an axisymmetric configuration of CM1. Therefore, given a decrease in θ with increasing radius in the modeled TCs, increased inflow ($v_{\rm rad} < 0$) is expected to produce a cooling effect. The area of peak cooling due to an increase in C_invrs_tau_shear coincides with a region of strengthened radial inflow (deep reds in Fig. 12b).

The response of the moisture cross section is tied to changes in vertical water vapor transport. In particular, moisture initially transported from the ocean to levels at or above 2000 m with less turbulent eddy dissipation (higher K_m) can

no longer reach those levels under a regime of higher eddy dissipation (lower K_m). As a result, water vapor is concentrated closer to the surface, thus explaining the moistening of the near-surface layer. This response is consistent with Bu et al. (2017), who defined the impact of turbulent mixing on the local water vapor (q) budget as follows (Bu et al. 2017):

$$\left[\frac{\partial q}{\partial t}\right]_{\text{mixing}} = -a \frac{\partial K_m}{\partial z}.$$
 (12)

Assuming a quasi-parabolic vertical profile of K_m (Fig. 11b), local drying exists at the lowest model levels below the peak

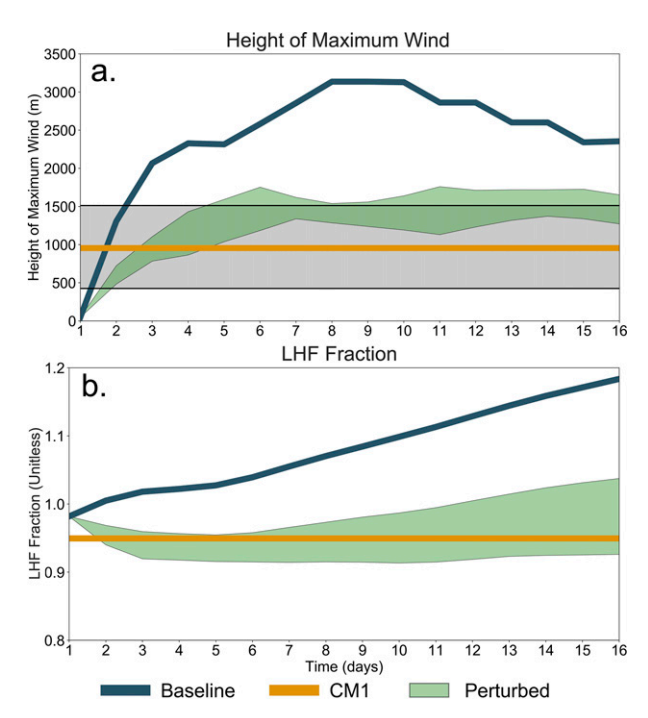


FIG. 15. Time series of the (a) height of maximum wind and (b) latent heat flux (LHF) fraction from CAM6-CLUBBX (dark blue) and CM1 (orange). Green shading denotes the range of values from a selection of perturbed configurations of CAM6-CLUBBX. Gray shading in (a) denotes the interquartile range of NOAA dropsonde observations of height of maximum wind. CAM6-CLUBBX time series come from an idealized configuration using an average of 20 ensemble members. The CM1 value in (a) comes from an axisymmetric configuration at steady state, while the value in (b) comes from a full 3D configuration (see supplemental material).

three configurations with (Fig. 16a) low, (Fig. 16b) moderate, and (Fig. 16c) high values of C_invrs_tau_shear (all other tunings constant). A higher value of $1/\tau_x$ implies greater dissipation of turbulent eddies due to the given process. In Fig. 16b, the background dissipation term (brown) is constant throughout the TC PBL, while the surface term (green) is largest near the surface where $z \to 0$. The shear term (blue) is maximized where vertical wind shear is highest, namely, near the surface and the jet maximum. The buoyancy dissipation term (pink) is small below 500-1000 m, where the PBL is well-mixed (Fig. 14a), but larger above the well-mixed layer where static stability (N^2) increases. Increasing C_invrs_tau_shear by a factor of 8 (Fig. 16a versus Figure 16c) produces appreciably greater eddy dissipation in areas of high wind shear. Meanwhile, the background term, which is independent of atmospheric conditions, and the surface term, which depends most strongly on height and surface roughness, do not appreciably change. However, the buoyancy term appears to increase, despite C_invrs_tau_N2 remaining constant between configurations, because increasing C_invrs_tau_shear increases N^2 near 1000 m (Fig. 12i). This provides another example of the nonlinear interactions between CLUBBX and thermodynamic profiles tied to the convective and microphysics schemes.

The diagnosis of L based on the $1/\tau$ eddy dissipation formulation allows flexibility in defining the turbulence profile because the shape of L is controlled by each of the eddy-dissipating processes in Eq. (6). For example, a uniform decrease in turbulent mixing could be achieved by increasing C_invrs_tau_bkgnd, while enhanced eddy dissipation applied to rough land surfaces could be achieved by increasing C_invrs_tau_sfc. The direct effects of increasing C_invrs_tau_shear and C_invrs_tau_N2 could similarly be isolated to high-shear (e.g., low-level jets, TCs) and stably stratified (e.g., polar regions, marine layers) environments. While this formulation of L is experimental, the MOAT analysis indicates that the C_invrs_tau terms are important targets for model improvements due to their physically based influence on PBL turbulence.

4. Conclusions

In this study, an SA is applied to assess the influence of perturbing various input parameters on TC structure in an idealized configuration of CESM2-CAM6 with an experimental version of CLUBB (CLUBBX). The comprehensive, yet computationally efficient, MOAT method varies N = 10 input parameters one-at-a-time over M = 15 separate paths and 165 total runs of CAM6-CLUBBX. The MOAT method describes the degree to which certain aspects of the TC PBL are sensitive to changes in the N = 10 inputs by calculating elementary effects of each input parameter on the output. The elementary effects are then used to derive several sensitivity metrics: μ_i^* , the average response of each input parameter; σ_i , the nonlinear effects of each input parameter; and f_{i+} , the frequency with which increasing the input parameter increases the output. We first analyze the degree of sensitivity (μ_i^*) and σ_i of the output metrics to the perturbed inputs and then quantify the frequency of positive and negative responses from f_{i+} . Potentially desirable input parameters have a high value of μ_i^* and a value of f_{j+} close to either 0 or 1. Inputs that meet these criteria afford model developers added confidence that changing the input will reliably alter the output in the desired manner. The MOAT method helps us isolate several highsensitivity input parameters (C14, C7_{upwp}, C_invrs_tau_sfc, and C_invrs_tau_shear) that, when increased, decrease vertical turbulent mixing in the TC PBL, which we find to be too high by default in CAM6-CLUBBX. One of these input parameters (C_invrs_tau_shear) is then gradually increased in CAM6-CLUBBX ensemble simulations. We show that increasing C_invrs_tau_shear, which is a coefficient tied to turbulent eddy dissipation by wind shear, reduces turbulent mixing and that this reduction in turbulent mixing influences other aspects of the TC PBL. In particular, the reduced turbulent mixing from increasing C_invrs_tau_shear lowers the height of maximum tangential wind, which is consistent with prior observational and modeling studies (Bryan 2012; Kepert 2001, 2012; Kepert and Wang 2001; Gopalakrishnan et al. 2013). Meanwhile, increasing C invrs tau shear reduces LHF fraction due to the impacts of reduced turbulent mixing on low-level temperature and moisture profiles, which is also consistent with prior studies (e.g., Bu et al. 2017; Kepert et al.

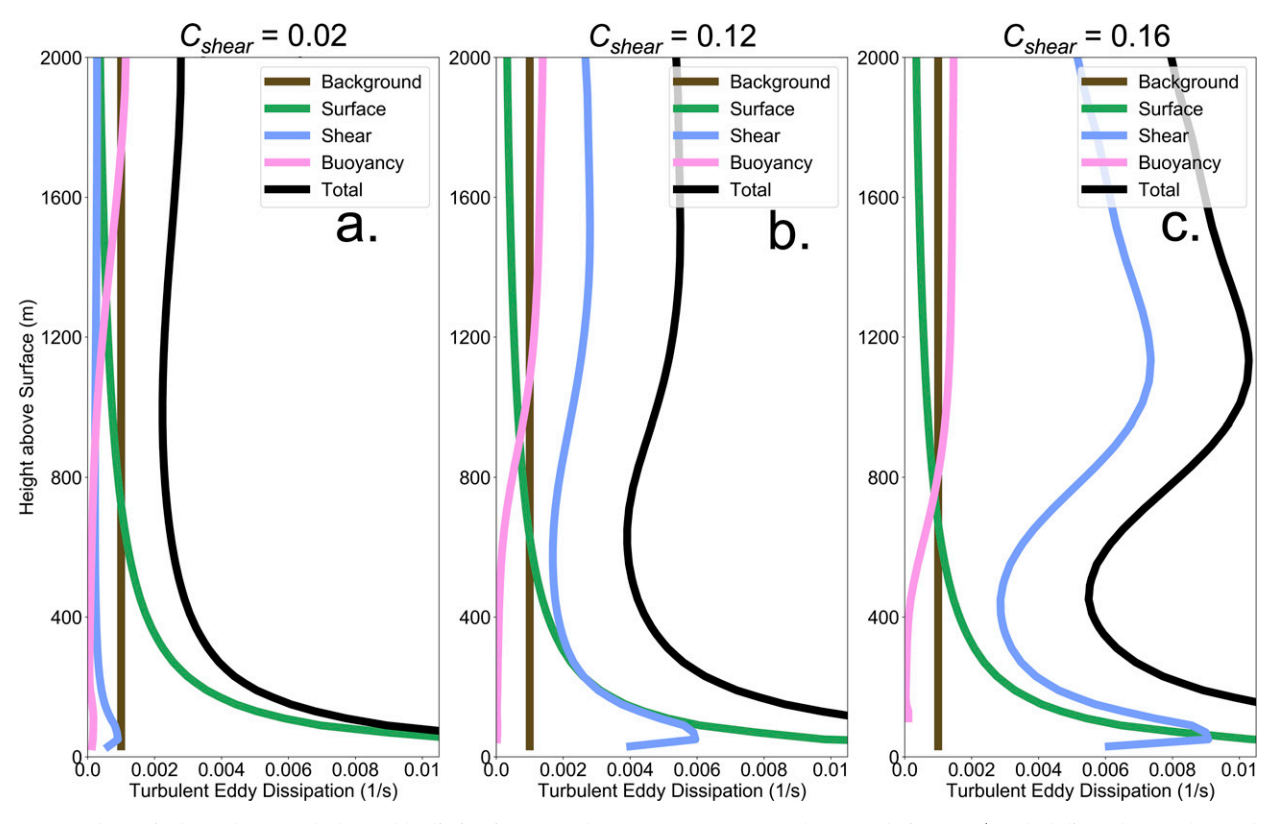


FIG. 16. Vertical profiles of turbulent eddy dissipation from the four components of the formulation of $1/\tau$. Black lines denote the total eddy dissipation from the four components. Each panel depicts a different idealized configuration of CAM6-CLUBBX with a unique value of C_invrs_tau_shear: (a) 0.02, (b) 0.12, and (c) 0.16. Profiles are averaged over 20 ensemble members at days 8, 10, and 12.

2016). Both effects act to correct high biases in height of maximum wind and LHF fraction in the baseline configuration of CAM6-CLUBBX. Finally, the MOAT analysis is used to inform the perturbation of multiple input parameters simultaneously. These multiperturbation configurations reduce CAM6-CLUBBX biases and bring the height of maximum wind and LHF fraction closer to observations.

From the analysis summarized above, we highlight the following key takeaways from this study:

- The baseline configuration of CAM6-CLUBBX exhibits a high bias in height of maximum tangential wind in idealized TCs because it is too diffusive. The baseline configuration is also too warm and dry in the lowest several hundred meters, resulting in a high bias in LHF fraction.
- 2) In concert with idealized or constrained model setups, the MOAT method is computationally efficient and objectively identifies high-sensitivity CLUBBX parameters that produce a strong, consistent directional response in various TC output metrics. In concert with physical interpretation and practical considerations of running a global ESM, the MOAT analysis can act as an initial tool to help identify a group of input parameters that deserve additional scrutiny as possible candidates for the attention of model developers.
- 3) The high-sensitivity input parameters effectively reduce CAM6-CLUBBX biases in height of maximum wind and LHF fraction compared to observations and CM1. In

- identifying multiple inputs, the MOAT method provides different pathways for bias reduction that model developers can weigh when choosing how to best improve CAM6-CLUBBX TC forecasts.
- 4) All N = 10 CLUBBX parameters explored in this study are tied to physical processes in the atmosphere, with the most sensitive processes tied to the production of turbulent mixing in the PBL. In addition, perturbing these parameters changes TC structure in ways that are consistent with past observational and modeling studies. Therefore, targeting these input parameters would make CAM6-CLUBBX's estimation of PBL turbulence more physically realistic.
- 5) The experimental CLUBBX formulation of turbulent length scale through the estimation of turbulent eddy dissipation has an influence on TC PBL structure, namely, through the C_invrs_tau_shear and C_invrs_tau_sfc coefficients. This formulation is advantageous because it allows the turbulence profile to be tailored to a specific atmospheric regime.

Though this study provides novel guidance to model users and developers, we note limitations that merit future research. First, while we anticipate wider applicability, it is unclear if these results also apply to a more realistic global configuration of CAM6-CLUBBX. In particular, it is important to assess whether the model improvements in the TC PBL come at the expense of errors in other parts of the global system. Second, it is important

to note that this analysis is not expected to fully correct all model biases. Though we demonstrate appreciable improvements in metrics like height of maximum wind and LHF fraction, other TC characteristics are not assessed here. Third, the MOAT method only examines the effects of changing a single parameter at-a-time, so the MOAT method may not be sufficient in cases where there are highly nonlinear interactions between input parameters (Campolongo et al. 2007). Therefore, a more thorough, yet computationally expensive, SA may be necessary for future research aimed at untangling the various nonlinear interactions between parameterizations of turbulence, convection, and microphysics. To this end, MOAT can serve as an initial screening tool to identify a smaller number of input parameters that merit additional scrutiny in a more computationally expensive SA.

The MOAT method provides a cost-effective means of assessing the impact of changing various input parameters without the need to run thousands of model simulations or resorting to hand-tuning (Hourdin et al. 2017). Building on prior studies (Covey et al. 2013; Morales et al. 2019), we use the MOAT method as a first step to objectively identify high-sensitivity input parameters that affect model output. The findings of this study demonstrate how the MOAT method can successfully identify such input parameters and provide critical, physically grounded guidance for model developers in reducing biases in how climate models depict TC PBL processes.

Acknowledgments. This research is jointly funded as part of a Climate Process Team (CPT) under Grant AGS-1916689 from the National Science Foundation (NSF) and Grant NA19OAR4310363 from the National Oceanic and Atmospheric Administration (NOAA). Computations for this research were performed on the Pennsylvania State University's Institute for Computational and Data Sciences' Roar supercomputer. We would also like to acknowledge highperformance computing support from Cheyenne (doi:10.5065/ D6RX99HX) provided by NCAR's Computational and Information Systems Laboratory, sponsored by the National Science Foundation. The Community Earth System Model version 2 is a joint effort between the National Center for Atmospheric Research (NCAR) and the University Corporation for Atmospheric Research (UCAR). Source code can be accessed at the following address: http://www.cesm.ucar.edu/models/cesm2/ release download.html. The specific release version of CESM2 (cesm2_2_beta05) with our modified CAM6-CLUBBX code can be accessed at the following address: https://github.com/ ESCOMP/CESM. Cloud Model 1 (CM1) was developed by G.H.B. at the NCAR-UCAR Mesoscale and Microscale Meteorology (MMM) Laboratory. Source code can be accessed at the following address: http://www2.mmm.ucar.edu/people/ bryan/cm1/. Dropsonde data comes from the NOAA Hurricane Research Division (HRD) Atlantic Oceanographic and Meteorological Laboratory (AOML): https://www.aoml.noaa.gov/hrd/ data_sub/dropsonde.html. Best track pressure-wind data comes from the NOAA NHC database: https://www.nhc.noaa.gov/data/ #hurdat.

REFERENCES

- Bacmeister, J. T., M. Wehner, R. Neale, A. Gettelman, C. Hannay, P. Lauritzen, J. Caron, and J. Truesdale, 2014: Exploratory high-resolution climate simulations using the Community Atmosphere Model (CAM). J. Climate, 27, 3073–3099, https:// doi.org/10.1175/JCLI-D-13-00387.1.
- —, K. Reed, C. Hannay, P. Lawrence, S. Bates, J. Truesdale, N. Rosenbloom, and M. Levy, 2018: Projected changes in tropical cyclone activity under future warming scenarios using a high-resolution climate model. *Climatic Change*, **146**, 547– 560, https://doi.org/10.1007/s10584-016-1750-x.
- Balaguru, K., and Coauthors, 2020: Characterizing tropical cyclones in the Energy Exascale Earth System Model Version 1.
 J. Adv. Model. Earth Syst., 12, e2019MS002024, https://doi.org/10.1029/2019MS002024.
- Bengtsson, L., K. Hodges, M. Esch, N. Keenlyside, L. Kornblueh, J. Luo, and T. Yamagata, 2007: How may tropical cyclones change in a warmer climate? *Tellus*, 59A, 539–561, https://doi. org/10.1111/j.1600-0870.2007.00251.x.
- Braun, S., and W. Tao, 2000: Sensitivity of high-resolution simulations of Hurricane Bob (1991) to planetary boundary layer parameterizations. *Mon. Wea. Rev.*, **128**, 3941–3961, https://doi.org/10.1175/1520-0493(2000)129<3941:SOHRSO>2. 0.CO:2.
- Bryan, G., 2012: Effects of surface exchange coefficients and turbulence length scales on the intensity and structure of numerically simulated hurricanes. *Mon. Wea. Rev.*, **140**, 1125–1143, https://doi.org/10.1175/MWR-D-11-00231.1.
- —, and R. Rotunno, 2009: The maximum intensity of tropical cyclones in axisymmetric numerical model simulations. *Mon. Wea. Rev.*, **137**, 1770–1789, https://doi.org/10.1175/ 2008MWR2709.1.
- —, R. Worsnop, J. Lundquist, and J. Zhang, 2017: A simple method for simulating wind profiles in the boundary layer of tropical cyclones. *Bound.-Layer Meteor.*, **162**, 475–502, https://doi.org/10.1007/s10546-016-0207-0.
- Bu, Y., R. Fovell, and K. Corbosiero, 2014: Influence of cloud-radiative forcing on tropical cyclone structure. *J. Atmos. Sci.*, 71, 1644–1662, https://doi.org/10.1175/JAS-D-13-0265.1.
- —, —, and —, 2017: The influences of boundary layer mixing and cloud-radiative forcing on tropical cyclone size. *J. Atmos. Sci.*, **74**, 1273–1292, https://doi.org/10.1175/JAS-D-16-0231.1.
- Bye, J., and A. Jenkins, 2006: Drag coefficient reduction at very high wind speeds. J. Geophys. Res., 111, C03024, https://doi. org/10.1029/2005JC003114.
- Camargo, S., and A. Wing, 2016: Tropical cyclones in climate models. Wiley Interdiscip. Rev.: Climate Change, 7, 211–237, https://doi.org/10.1002/wcc.373.
- —, and Coauthors, 2020: Characteristics of model tropical cyclone climatology and the large-scale environment. *J. Climate*, 33, 4463–4487, https://doi.org/10.1175/JCLI-D-19-0500.1.
- Campolongo, F., J. Cariboni, and A. Saltelli, 2007: An effective screening design for sensitivity analysis of large models. *Envi*ron. *Modell. Software*, 22, 1509–1518, https://doi.org/10.1016/j. envsoft.2006.10.004.
- Chen, J., and S. Linn, 2011: The remarkable predictability of inter-annual variability of Atlantic hurricanes during the past decade. *Geophys. Res. Lett.*, 38, L11804, https://doi.org/10. 1029/2011GL047629.

- —, and —, 2013: Seasonal predictions of tropical cyclones using a 25-km-resolution general circulation model. *J. Climate*, **26**, 380–398, https://doi.org/10.1175/JCLI-D-12-00061.1.
- Covey, C., D. Lucas, J. Tannahill, X. Garaizar, and R. Klein, 2013: Efficient screening of climate model sensitivity to a large number of perturbed input parameters. J. Adv. Model. Earth Syst., 5, 598–610, https://doi.org/10.1002/jame.20040.
- Davis, C. A., 2018: Resolving tropical cyclone intensity in models. Geophys. Res. Lett., 45, 2082–2087, https://doi.org/10.1002/ 2017GL076966.
- Donelan, M., B. Haus, N. Reul, W. Plant, M. Stiassnie, H. Graber, O. Brown, and E. Saltzman, 2004: On the limiting aerodynamic roughness of the ocean in very strong winds. *Geophys. Res. Lett.*, 31, L18306, https://doi.org/10.1029/2004GL019460.
- Emanuel, K., 1986: The air-sea interaction theory for tropical cyclones. Part I: Steady-state maintenance. J. Atmos. Sci., 43, 585–605, https://doi.org/10.1175/1520-0469(1986)043<0585: AASITF>2.0.CO:2.
- Fovell, R., Y. Bu, K. Corbosiero, W. Tung, Y. Cao, H. Kuo, L. Hsu, and H. Su, 2016: Influence of cloud microphysics and radiation on tropical cyclone structure and motion. *Multiscale Convection-Coupled Systems in the Tropics: A Tribute to Dr. Michio Yanai, Meteor. Monogr.*, Vol. 56, Amer. Meteor. Soc., https://doi.org/10.1175/AMSMONOGRAPHS-D-15-0006.1.
- French, J., W. Drennan, J. Zhang, and P. Black, 2007: Turbulent fluxes in the hurricane boundary layer. Part I: Momentum flux. J. Atmos. Sci., 64, 1089–1102, https://doi.org/10.1175/ JAS3887.1.
- Golaz, J., V. Larson, and W. Cotton, 2002: A PDF-based model for boundary layer clouds. Part I: Method and model description. J. Atmos. Sci., 59, 3540–3551, https://doi.org/10.1175/ 1520-0469(2002)059<3540:APBMFB>2.0.CO:2.
- Gopalakrishnan, S., F. Marks Jr., J. A. Zhang, X. Zhang, J.-W. Bao, and V. Tallapragada, 2013: A study of the impacts of vertical diffusion on the structure and intensity of the tropical cyclones using the high-resolution HWRF system. *J. Atmos. Sci.*, 70, 524–541, https://doi.org/10.1175/JAS-D-11-0340.1.
- —, A. Hazelton, and J. A. Zhang, 2021: Improving hurricane boundary layer parameterization scheme based on observations. *Earth Space Sci.*, 8, e2020EA001422, https://doi.org/10. 1029/2020EA001422.
- Guo, Z., and Coauthors, 2014: A sensitivity analysis of cloud properties to CLUBB parameters in the Single-Column Community Atmosphere Model (SCAM5). J. Adv. Model. Earth Syst., 6, 829–858, https://doi.org/10.1002/2014MS000315.
- —, B. M. Griffin, S. Domke, and V. E. Larson, 2021: A parameterization of turbulent dissipation and pressure damping time scales in stably stratified inversions, and its effects on low clouds in global simulations. *J. Adv. Model. Earth Syst.*, 13, e2020MS002278, https://doi.org/10.1029/2020MS002278.
- Held, I., and M. Zhao, 2008: Horizontally homogeneous rotating radiative-convective equilibria at GCM resolution. *J. Atmos.* Sci., 65, 2003–2013, https://doi.org/10.1175/2007JAS2604.1.
- Herman, J., and W. Usher, 2017: SALib: An open-source Python library for sensitivity analysis. J. Open Source Software, 2, 97, https://doi.org/10.21105/joss.00097.
- —, J. Kollat, P. Reed, and T. Wagener, 2013: Technical note: Method of Morris effectively reduces the computational demands of global sensitivity analysis for distributed watershed models. *Hydrol. Earth Syst. Sci.*, 17, 2893–2903, https:// doi.org/10.5194/hess-17-2893-2013.

- Hourdin, F., and Coauthors, 2017: The art and science of climate model tuning. *Bull. Amer. Meteor. Soc.*, 98, 589–602, https://doi.org/10.1175/BAMS-D-15-00135.1.
- Kepert, J., 2001: The dynamics of boundary layer jets within the tropical cyclone core. Part I: Linear theory. J. Atmos. Sci., 58, 2469–2484, https://doi.org/10.1175/1520-0469(2001)058<2469: TDOBLJ>2.0.CO;2.
- —, 2012: Choosing a boundary layer parameterization for tropical cyclone modeling. *Mon. Wea. Rev.*, **140**, 1427–1445, https://doi.org/10.1175/MWR-D-11-00217.1.
- —, and Y. Wang, 2001: The dynamics of boundary layer jets within the tropical cyclone core. Part II: Linear enhancement. J. Atmos. Sci., 58, 2485–2501, https://doi.org/10.1175/1520-0469(2001)058<2485:TDOBLJ>2.0.CO;2.
- —, J. Schwendike, and H. Ramsay, 2016: Why is the tropical cyclone boundary layer not "well mixed"? J. Atmos. Sci., 73, 957–973, https://doi.org/10.1175/JAS-D-15-0216.1.
- Khairoutdinov, M., and K. Emanuel, 2013: Rotating radiative-convective equilibrium simulated by a cloud-resolving model. J. Adv. Model. Earth Syst., 5, 816–825, https://doi.org/10.1002/2013MS000253.
- Large, W., and S. Pond, 1981: Open ocean momentum flux measurements in moderate to strong winds. J. Phys. Oceanogr., 11, 324–336, https://doi.org/10.1175/1520-0485(1981)011<0324: OOMFMI>2.0.CO;2.
- —, and S. Yeager, 2009: The global climatology of an interannually varying air-sea flux data set. *Climate Dyn.*, 33, 341–364, https://doi.org/10.1007/s00382-008-0441-3.
- Larson, V., 2020: CLUBB-SILHS: A parameterization of subgrid variability in the atmosphere. J. Adv. Model. Earth Syst., https://arxiv.org/abs/1711.03675.
- —, S. Domke, and B. Griffin, 2019: Momentum transport in shallow cumulus clouds and its parameterization by higherorder closure. *J. Adv. Model. Earth Syst.*, 11, 3419–3442, https://doi.org/10.1029/2019MS001743.
- Lee, C., S. Camargo, F. Vitart, A. Sobel, J. Camp, S. Wang, M. Tippett, and Q. Yang, 2020: Subseasonal predictions of tropical cyclone occurrence and ACE in the S2S dataset. *Mon. Wea. Rev.*, 35, 921–938, https://doi.org/10.1175/WAF-D-19-02171
- Li, X., and Z. Pu, 2020: Vertical eddy diffusivity parameterization based on a large eddy simulation and its impact on prediction of hurricane landfall. *Geophys. Res. Lett.*, 48, e2020GL090703, https://doi.org/10.1029/2020GL090703.
- Makin, V., 2005: A note on the drag of the sea surface at hurricane winds. *Bound.-Layer Meteor.*, **115**, 169–176, https://doi.org/10.1007/s10546-004-3647-x.
- Mauritsen, T., and L. Enger, 2008: On the use of shear-dependent turbulent length-scales. *Quart. J. Roy. Meteor. Soc.*, **134**, 539–540, https://doi.org/10.1002/qj.218.
- Moon, I., I. Ginis, and T. Hara, 2008: Impact of reduced drag coefficient on ocean wave modeling under hurricane conditions. *Mon. Wea. Rev.*, 136, 1217–1223, https://doi.org/10.1175/ 2007MWR2131.1.
- Moon, Y., and Coauthors, 2020: Azimuthally averaged wind and thermodynamic structures of tropical cyclones in global climate models and their sensitivity to horizontal resolution. *J. Climate*, 33, 1575–1595, https://doi.org/10.1175/JCLI-D-19-0172.1.
- Morales, A., D. Posselt, H. Morrison, and F. He, 2019: Assessing the influence of microphysical and environmental parameter perturbations on orographic precipitation. *J. Atmos. Sci.*, 76, 1373–1395, https://doi.org/10.1175/JAS-D-18-0301.1.

- Morris, M., 1991: Factorial sampling plans for preliminary computational experiments. *Technometrics*, 33, 161–174, https://doi.org/10.1080/00401706.1991.10484804.
- Murakami, H., G. Vecchi, S. Underwood, and T. Delworth, 2015: Simulation and prediction of category-4 and -5 hurricanes in the high-resolution GFDL HiFLOR coupled climate model. *J. Climate*, 28, 9058–9079, https://doi.org/10.1175/JCLI-D-15-0216.1.
- —, G. Villarini, G. Vecchi, W. Zhang, and R. Gudgel, 2016: Statistical-dynamical seasonal forecast of North Atlantic and U.S. landfalling tropical cyclones using the high-resolution GFDL FLOR coupled model. *Mon. Wea. Rev.*, **144**, 2101–2123, https://doi.org/10.1175/MWR-D-15-0308.1.
- Nolan, D., D. Stern, and J. Zhang, 2009a: Evaluation of planetary boundary layer parameterizations in tropical cyclones by comparison of in situ observations and high-resolution simulations of Hurricane Isabel (2003). Part II: Inner-core boundary layer and eyewall structure. *Mon. Wea. Rev.*, 137, 3675– 3698, https://doi.org/10.1175/2009MWR2786.1.
- —, J. Zhang, and D. Stern, 2009b: Evaluation of planetary boundary layer parameterizations in tropical cyclones by comparison of in situ observations and high-resolution simulations of Hurricane Isabel (2003). Part I: Initialization, maximum winds, and the outer-core boundary layer. *Mon. Wea. Rev.*, 137, 3651–3674, https://doi.org/10.1175/2009MWR2785.1.
- Persing, J., M. Montgomery, J. McWilliams, and R. Smith, 2013: Asymmetric and axisymmetric dynamics of tropical cyclones. *Atmos. Chem. Phys.*, 13, 12299–12341, https://doi.org/10.5194/acp-13-12299-2013.
- Powell, M., P. Vickery, and T. Reinhold, 2003: Reduced drag coefficient for high wind speeds in tropical cyclones. *Nature*, 422, 279–283, https://doi.org/10.1038/nature01481.
- Randall, D. A., and Coauthors, 2007: Climate models and their evaluation. Climate Change 2007: The Physical Science Basis, S. Solomon et al., Eds., Cambridge University Press, 589–662.
- Reed, K., and C. Jablonowski, 2012: Idealized tropical cyclone simulations of intermediate complexity: A test case for AGCMs. J. Adv. Model. Earth Syst., 4, M04001, https://doi. org/10.1029/2011MS000099.
- —, and D. Chavas, 2015: Uniformly rotating global radiative-convective equilibrium in the Community Atmosphere Model, version 5. *J. Adv. Model. Earth Syst.*, 7, 1938–1955, https://doi.org/10.1002/2015MS000519.
- Richter, D., C. Wainwright, D. Stern, G. Bryan, and D. Chavas, 2021: Potential low bias in high-wind drag coefficient inferred from dropsonde data in hurricanes. *J. Atmos. Sci.*, 78, 2339– 2352, https://doi.org/10.1175/JAS-D-20-0390.1.
- Roberts, M., and Coauthors, 2020a: Impact of model resolution on tropical cyclone simulation using HighResMIP-PRIMA-VERA multimodel ensemble. *J. Climate*, **33**, 2557–2583, https://doi.org/10.1175/JCLI-D-19-0639.1.
- —, and Coauthors, 2020b: Projected future changes in tropical cyclones using the CMIP6 HighResMIP multimodel ensemble. *Geophys. Res. Lett.*, 47, e2020GL088662, https://doi.org/ 10.1029/2020GL088662.
- Shi, X., and C. Bretherton, 2014: Large-scale character of an atmosphere in rotating radiative-convective equilibrium. J. Adv. Model. Earth Syst., 6, 616–629, https://doi.org/10.1002/ 2014MS000342.
- Smith, R., and G. Thomsen, 2010: Dependence of tropical-cyclone intensification on the boundary-layer representation in a numerical model. *Quart. J. Roy. Meteor. Soc.*, **136**, 1671– 1685, https://doi.org/10.1002/qj.687.

- Ueda, H., T. Fukui, M. Kajino, M. Horiguchi, H. Hashiguchi, and S. Fukao, 2012: Eddy diffusivities for momentum and heat in the upper troposphere and lower stratosphere measured by MU radar and RASS, and a comparison of turbulence model predictions. *J. Atmos. Sci.*, 69, 323–337, https://doi.org/10. 1175/JAS-D-11-023.1.
- Vecchi, G., and Coauthors, 2014: On the seasonal forecasting of regional tropical cyclone activity. J. Climate, 27, 7994–8016, https://doi.org/10.1175/JCLI-D-14-00158.1.
- Vitart, F., A. Leroy, and M. Wheeler, 2010: A comparison of dynamical and statistical predictions of weekly tropical cyclone activity in the Southern Hemisphere. *Mon. Wea. Rev.*, 138, 3671–3682, https://doi.org/10.1175/2010MWR3343.1.
- Walsh, K., and Coauthors, 2015: Hurricanes and climate: The U.S. CLIVAR Working Group on Hurricanes. *Bull. Amer. Meteor.* Soc., 96, 997–1017, https://doi.org/10.1175/BAMS-D-13-00242.1.
- Wehner, M., and Coauthors, 2014: The effect of horizontal resolution on simulation quality in the Community Atmosphere Model (CAM5.1). J. Adv. Model. Earth Syst., 6, 980–997, https://doi.org/10.1002/2013MS000276.
- Wilks, D. S., 2011: Statistical Methods in the Atmospheric Sciences.
 3rd ed. International Geophysics Series, Vol. 100, Academic Press, 704 pp.
- Wing, A., K. Reed, M. Satoh, B. Stevens, S. Bony, and T. Ohno, 2018: Radiative-convective equilibrium model intercomparison project. *Geosci. Model Dev.*, 11, 793–813, https://doi.org/ 10.5194/gmd-11-793-2018.
- —, and Coauthors, 2019: Moist static energy budget analysis of tropical cyclone intensification in high-resolution climate models. *J. Climate*, 32, 6071–6095, https://doi.org/10.1175/ JCLI-D-18-0599.1.
- Zarzycki, C., 2016: Tropical cyclone intensity errors associated with lack of two-way ocean coupling in high-resolution global simulations. J. Climate, 29, 8589–8610, https://doi.org/10.1175/ JCLI-D-16-0273.1.
- —, and C. Jablonowski, 2014: A multidecadal simulation of Atlantic tropical cyclones using a variable-resolution global atmospheric general circulation model. *J. Adv. Model. Earth* Syst., 6, 805–828, https://doi.org/10.1002/2014MS000352.
- —, and —, 2015: Experimental tropical cyclone forecasts using a variable-resolution global model. *Mon. Wea. Rev.*, 143, 4012–4037, https://doi.org/10.1175/MWR-D-15-0159.1.
- —, and P. Ullrich, 2017: Assessing sensitivities in algorithmic detection of tropical cyclones in climate data. *Geophys. Res. Lett.*, 44, 1141–1149, https://doi.org/10.1002/2016GL071606.
- —, C. Jablonowski, and M. Taylor, 2014a: Using variable-resolution meshes to model tropical cyclones in the Community Atmosphere Model. *Mon. Wea. Rev.*, **142**, 1221–1239, https://doi.org/10.1175/MWR-D-13-00179.1.
- —, M. Levy, and C. Jablonowski, 2014b: Aquaplanet experiments using CAM's variable-resolution dynamical core. *J. Climate*, 27, 5481–5503, https://doi.org/10.1175/JCLI-D-14-00004.1.
- Zhang, F., and X. Pu, 2017: Effects of vertical eddy diffusivity parameterization on the evoluation of landfalling hurricanes. J. Atmos. Sci., 74, 1879–1905, https://doi.org/10.1175/JAS-D-16-0214.1.
- Zhang, J., and W. Drennan, 2012: An observational study of vertical eddy diffusivity in the hurricane boundary layer. J. Atmos. Sci., 69, 3223–3236, https://doi.org/10.1175/JAS-D-11-0348.1.
- —, F. Marks, M. Montgomery, and S. Lorsolo, 2011: An estimation of turbulent characteristics in the low-level

region of intense Hurricanes Allen (1980) and Hugo (1989). *Mon. Wea. Rev.*, **139**, 1447–1462, https://doi.org/10.1175/2010MWR3435.1.

Zhang, W., and Coauthors, 2016: Improved simulation of tropical cyclone responses to ENSO in the western North Pacific in the high-resolution GFDL HiFLOR coupled climate model.

J. Climate, 29, 1391–1415, https://doi.org/10.1175/JCLI-D-15-0475 1

Zhou, W., I. Held, and S. Garner, 2014: Parameter study of tropical cyclones in rotating radiative-equilibrium with column physics and resolution of a 25-km GCM. J. Atmos. Sci., 71, 1058–1069, https://doi.org/10.1175/JAS-D-13-0190.1.